Journal of Theoretical Biology 524 (2021) 110733

Contents lists available at ScienceDirect

Journal of Theoretical Biology

journal homepage: www.elsevier.com/locate/yjtbi

Matrix adhesion and remodeling diversifies modes of cancer invasion across spatial scales

D. Pramanik [a,b], M.K. Jolly [b,*], R. Bhat [a,*]

[a] Department of Molecular Reproduction, Development and Genetics, Indian Institute of Science, Bangalore 560012, India
[b] Centre for BioSystems Science and Engineering, Indian Institute of Science, Bangalore 560012, India

ARTICLE INFO

Article history:
Received 22 July 2020
Revised 14 April 2021
Accepted 16 April 2021
Available online 30 April 2021

Keywords:
Extracellular matrix
Invasion
Basement membrane
Cellular Potts model

ABSTRACT

The metastasis of malignant epithelial tumors begins with the egress of transformed cells from the confines of their basement membrane (BM) to their surrounding collagen-rich stroma. Invasion can be morphologically diverse: when breast cancer cells are separately cultured within BM-like matrix, collagen I (Coll I), or a combination of both, they exhibit collective-, dispersed mesenchymal-, and a mixed collective-dispersed (multimodal)- invasion, respectively. In this paper, we asked how distinct these invasive modes are with respect to the cellular and microenvironmental cues that drive them. A rigorous computational exploration of invasion was performed within an experimentally motivated Cellular Potts-based modeling environment. The model comprised of adhesive interactions between cancer cells, BM- and Coll I-like extracellular matrix (ECM), and reaction–diffusion-based remodeling of ECM. The model outputs were parameters cognate to dispersed- and collective- invasion. A clustering analysis of the output distribution curated through a careful examination of subsumed phenotypes suggested at least four distinct invasive states: dispersed, papillary-collective, bulk-collective, and multimodal, in addition to an indolent/non-invasive state. Mapping input values to specific output clusters suggested that each of these invasive states are specified by distinct input signatures of proliferation, adhesion and ECM remodeling. In addition, specific input perturbations allowed transitions between the clusters and revealed the variation in the robustness between the invasive states. Our systems-level approach proffers quantitative insights into how the diversity in ECM microenvironments may steer invasion into diverse phenotypic modes during early dissemination of breast cancer and contributes to tumor heterogeneity.

1. Introduction

The details of the beginnings of cancer progression determine not just the kinetics of its metastasis but also its response to therapeutic efforts (Haeger et al., 2020; Nieto et al., 2016). Transformed cells of epithelial cancers, such as those of breast and prostate, proliferate and breach their covering laminin-rich basement membrane (BM) barriers to migrate to the surrounding stromal connective tissue consisting of fibroblasts, other resident cells, and extracellular matrix (ECM) (Nelson and Bissell, 2005; Pally et al., 2019; Pickup et al., 2014). The latter is rich in fibrillar collagens, especially Coll I, other fibrillar glycoproteins and proteoglycans (Di Lullo et al., 2002; Hynes, 2009).

Reciprocal regulation between cancer cells and their surrounding tissue microenvironment (such as the adhesion of cells to, and their degradation of, ECM, on the one hand and effect of the porosity, crosslinking and density of the ECM on the other) determine the nature of their migration (Anderson, 2005; Jain et al., 2020; Nissen et al., 2019; Vedula et al., 2012) Invasion of tumor epithelia from breast, (but also applied generally to adenocarcinomas) has been broadly described as comprising distinct modes ranging from dispersed unicellular to multicellular categories (Roussos et al., 2011). Solitary breast cancer epithelia have been shown to disperse and migrate through mammary ECM in a fibroblast-like manner (Madsen and Sahai, 2010). Such a migration pattern concurs with a series of changes in gene expression, intercellular adhesion and cell shape, known as the epithelial to mesenchymal transition or EMT (van Zijl et al., 2011). The spindle-shaped mammary 'mesenchymal' cells interact extensively with ECM in their process of migration (unlike the other unicellular migratory mode: amoeboid, where the adhesion with matrix is less crucial) (Friedl et al., 2004; Gadea et al., 2008; Huang et al., 2014; Paňková et al., 2010; Sanz-Moreno et al., 2008). On the other hand, collective invasion involves migration of ensembles of breast tumor epithelia that

* Corresponding authors.
E-mail addresses: pramanik.durjay.01@gmail.com (D. Pramanik), mkjolly@iisc.ac.in (M.K. Jolly), ramray@iisc.ac.in (R. Bhat).

https://doi.org/10.1016/j.jtbi.2021.110733
0022-5193/

may retain adhesive and communicative contacts with each other (Cheung et al., 2013; Friedl et al., 2012; Vedula et al., 2014), although confinement by ECM could jam unadhered mesenchymal cells to also migrate in a collective fashion (Ilina et al., 2020). These diverse phenotypes are also reflected in blood-borne dissemination of circulating tumor cells as individual cells or multicellular clusters (Aceto et al., 2014; Bocci et al., 2019).

The migratory dynamics of breast cancer epithelia may also transition among the above-mentioned types and drive phenotypic heterogeneity and symbiotic behavior in cancer invasion patterns (Hecht et al., 2015; Huang et al., 2015; Ilina et al., 2018; Lintz et al., 2017). As cancer cells migrate to newer microenvironments, transitions from mesenchymal to epithelial morphologies could appropriately render invasive single cells more adhesive to each other (Krakhmal et al., 2015). Collectively migrating strands of cells are typically thought of as hybrid epithelial/mesenchymal (E/M) phenotype (Nagai et al., 2020); in vitro, *in vivo* and *in silico* evidence for existence, plasticity and aggressiveness of such hybrid E/M cells across cancers has been mounting (Jolly et al., 2019). Thus, it is not surprising to identify unique migratory behaviors of neoplastic cells that are phenotypically intermediate between their dispersed and collective counterparts; for instance, multicellular streaming of amoeboid or mesenchymal cells (Friedl et al., 2012; Kedrin et al., 2008; Liu et al., 2019; Patsialou et al., 2013) driven by weak intercellular junction strength. Studies on breast cancer progression of the jamming-unjamming transition regulated by heterogeneity show that material properties of ECM may also lead to transitions in migratory modes (Sadati et al., 2013). In fact, Friedl and coworkers have come up with a three-dimensional graph showing how the three axes of leading-edge polarity, apicobasal polarity and cell–cell contacts can accommodate the different modes of phenotypes. This idea is based on an earlier review on the same topic where they argue for a "multiparameter tuning model of invasion wherein a combination of cues such as density, stiffness, and orientation of the extracellular matrix together with cell determinants—including cell–cell and cell–matrix adhesion, cytoskeletal polarity and stiffness, and pericellular proteolysis—interdependently control migration mode and efficiency" (Friedl and Wolf, 2008; Wolf et al., 2007).

Given the multifactorial nature of phenomena influencing tumor progression across diverse scales, it is not surprising that the latter has enjoyed a long and rich tradition of investigation through mathematical modeling (Alarcón et al., 2004; Araujo and McElwain, 2004). These models can be classified as on-lattice (cells tracked along a rigid mesh) or off-lattice (no such mesh used). Cellular automata, cellular Potts, and lattice-gas cellular automata (LGCA) models are all examples of lattice-based models, while vertex-based and subcellular element-based models are instance of off-lattice ones (Metzcar et al., 2019; Scianna and Preziosi, 2013). In such frameworks, the behavior of individual cells, cell–cell interactions and cell-matrix interactions can be investigated within constructed tissue-like environments (Anderson, 2005; Anderson et al., 2007; Scianna et al., 2013). Recent frameworks have also integrated continuous (diffusible nutrients or growth factors) and discrete (individual cells – tumor, stromal) variables over multiple time and length scales (Chamseddine and Rejniak, 2020). Boghaert and coworkers have used a lattice-based model to demonstrate how an interplay in rates of proliferation and apoptosis leads to distinct morphological transitions between ductal carcinoma in situ (DCIS) and invasive ductal carcinoma (IDC) (Boghaert et al., 2014). The analysis of specific cellular biochemical modules and biomechanics and their integration with lattice-based multicellular dynamics has allowed a better understanding of invasion and transitions between its distinct modes (Andasari et al., 2012). Simulations using an individual-based multiscale model have shown how intercellular adhesion driven through E-cadherin and its regulation by β-catenin regulates EMT and impacts cell migration (Ramis-Conde et al., 2008). Recently, elegant efforts to incorporate the influence of the stroma of cancer invasion incorporate the effects of the urokinase-type plasminogen activator (uPA) system (consisting of uPA, its inhibitors) using both a PDE-based approach (Andasari et al., 2011) and a multiscale moving boundary framework (Peng et al., 2017). A more recent numerical-based analysis based on uPA-guided cancer cell invasion shows how the interplay between uPA and its inhibitors lead to sporadic invasion patterns (Hodgkinson et al., 2018).

An increasing number of models have thus incorporated cell invasion as a function of cell–cell adhesion and cell-matrix adhesion (Bearer et al., 2009; Szabo and Merks, 2013). Discrete approaches such as agent- or cell-based ones to study cancer invasion have the advantage of modularizing interactions between the cells and their environment, thus allowing quick transitions from mechanistic hypothesis-framing to rule-based behaviors on single-cell and cell-population scales (Allena et al., 2016; Metzcar et al., 2019). Recent efforts grounded in continuum approaches and lattice growth cellular automaton (LGCA) framework have revealed how heterogeneity in cell–cell adhesion (as a result of many possible reasons: genetic, epigenetic and/or microenvironmental control of EMT or through spatiotemporal variation in cell- and matrix-adhesion dynamics) can pattern the dissemination of cancer cells (Domschke et al., 2014; Reher et al., 2017). Another study combined experiments with simulations to showcase a feedback loop between cell contractility, and the alignment of collagen fibers to posit that intermediate matrix stiffness is optimal for invasion (Ahmadzadeh et al., 2017), thereby emphasizing the nonlinear nature of ECM behavior in determining cancer cell invasion. ECM density and organization, as a function of MMP density, can regulate the switch between proteolytic and non-proteolytic modes of breast cancer invasion (Kumar et al., 2016). However, the existent literature on invasion, to the best of our knowledge, has not yet explicitly investigated the distinctions and commonalities between mechanisms underlying collective and dispersed modes of invasion. In consequence, phenomena such as mesenchymal streaming in the context of mammary tumors (Friedl et al., 2012) and tumor budding in the case of colorectal malignancies (Prall, 2007), which have been meticulously described in pathological and surgical literature, remain largely uninvestigated via mathematical modeling approaches.

Using an experimental setup that mimicked the topographical arrangement of invasive cell clusters encapsulated within BM-like ECM and subsequently by Coll I, we have been able to observe the co-occurrence of invasion across multiple scales, ((Pally et al., 2019), of note, also observed through intravital microscopy of invading breast tumors (Ilina et al., 2018)). These experimental observations were simulated using Compucell3D, a modeling framework based on the Cellular Potts model (Das et al., 2017; Glazier and Graner, 1993; Graner and Glazier, 1992; Swat et al., 2012; Zhang et al., 2011). Our simulations suggested that an interplay between cell–cell and cell-ECM adhesion, cell proliferation and reaction–diffusion-based modulation of matrix proteolysis (computational equivalents of the ECM-degrading matrix metalloproteinases (MMPs) and their inhibitors (The inhibitors of matrix metalloproteinases or TIMPs))-, can give rise to dispersed, collective, and hybrid (multimodal) invasive phenotypes. In this manuscript, we undertake a rigorous investigation of the diversity of invasive phenotypes brought about through the concerted interplay of the above-mentioned cellular phenomena. Our multiparametric simulations followed by statistical analyses suggest four distinct invasive states (in addition to an indolent/noninvasive state) within this breast cancer-motivated framework. We explore the inputs that maintain such invasive modes and enable possible interconversions among them, the targeting of which represents insights into novel therapeutic strategies in the future.

2. Results

2.1. Construction of an invasion phenotypic space based on the dynamics of reaction–diffusion, and cell–cell and -matrix adhesion

Experiments of breast cancer cells in diverse ECM environments show distinct invasive modes in fibrillar matrix (Coll I), non-fibrillar matrix (BM) and a topologically radial arrangement of both. We began by asking whether we could simulate the above-mentioned diverse invasive patterns using a computational model, that simulated cell–cell and -ECM (BM and Coll I) adhesion, and reaction–diffusion kinetics of MMP- and TIMP-based ECM remodeling (Fig. 1A; all the model interactions depicted schematically in Fig. 1B; for further details, please refer to the section titled modeling framework). In this model, we allowed the cells to proliferate and migrate actively in response to chemoattraction from the degraded fibrillar collagenous ECM (Fang et al., 2014; O'Brien et al., 2010; Postlethwaite et al., 1978; Xu et al., 2019) (Fig. 1B). For a given set of parameters, we also observed exclusively collective and dispersed mesenchymal invasion, when only BM or only Coll I-like ECM surrounded the clusters (Supplementary Fig. 1). When both ECMs were present, the model predicted phenotypes with exclusive as well as concurrent presence of both migratory modes exhibiting a close correspondence with experiments (Fig. 2A).

To better quantify the invasion phenotype and characterize the tendency of cells to switch among these phenotypes, we constructed an invasion phenotypic space, wherein the horizontal and vertical axes represent the metrics inherent to collective and dispersed cellular invasion respectively (Fig. 2B). Therefore, the X axis denoted the size of the largest single multicellular mass (the starting 'primary focus') at the end of the simulation. The Y axis denoted the number of objects (cells or small cellular clusters) that are spatially disconnected or dispersed from the primary focal mass at the end of the simulation. Outputs that were closer to X axis therefore represented collective migration; those closer to Y axis represented dispersed cells/clusters migrating solitarily upon disaggregation from the focal multicellular mass. Outputs with a relatively higher magnitude of values on X and Y axes were prognostic of multimodal invasive morphologies.

Based on our previous simulation results, we took the following inputs to map the phenotypic space: a) the contact energies representing cell–cell, cell-BM and cell-collagen adhesion, b) cell division, c) diffusivity of MMP and d) the cooperativity between MMP and its diffusible inhibitor TIMP (the threshold ratio of MMP to TIMP concentration at a given spatial point that is required to degrade Coll I, which was shown to be an important regulator of multimodal invasion (Diambra et al., 2015; Pally et al., 2019)) (Fig. 1A). We chose the input values for which we observed exclusive dispersed, or collective invasion phenotypes and then progressively decreased them in discrete intervals to a minimum limit at which no invasion was observed. In total, five values of each input were chosen (equivalently spaced apart with the extreme values determined through pilot simulations where invasion was respectively, minimal and prolific; outputs were computed for all combinations of input values; the computation was repeated 3 times (replicates) using CompuCell3D. The replicates aim to capture the variability in cellular responses enabled by the underlying stochastic framework of the Cellular Potts modeling framework. These outputs were mapped onto the 2D invasion phenotypic space (Fig. 2C). The distribution of outputs as a function of our input parameter variation suggested a phenomenological continuity between invasive modes. Whereas our output method does not enable the identification of optimal parametric combinations

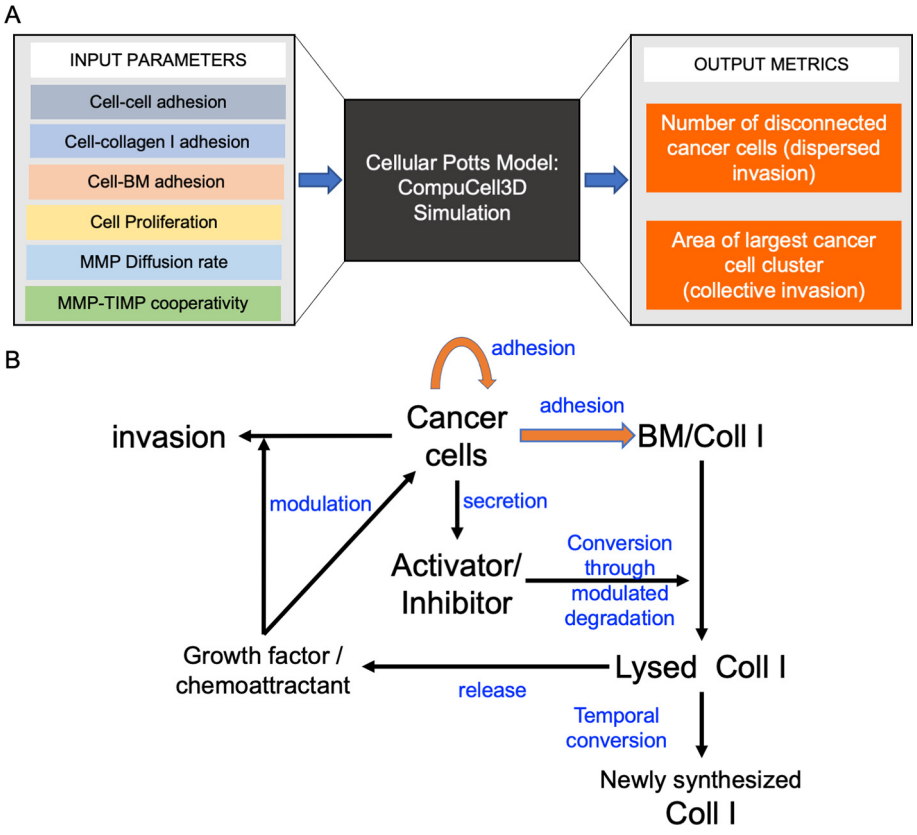

Fig. 1. Introduction to the computational framework, simulation inputs and output phenotypic space (A) Schematic depiction of the input variables that have been deployed in the CompuCell 3D simulations. The result of the simulations was computed as two outputs that are representative of dispersed invasion and collective invasion. (B) Schematic depiction of the interactions between the components of our computational model of invasion.

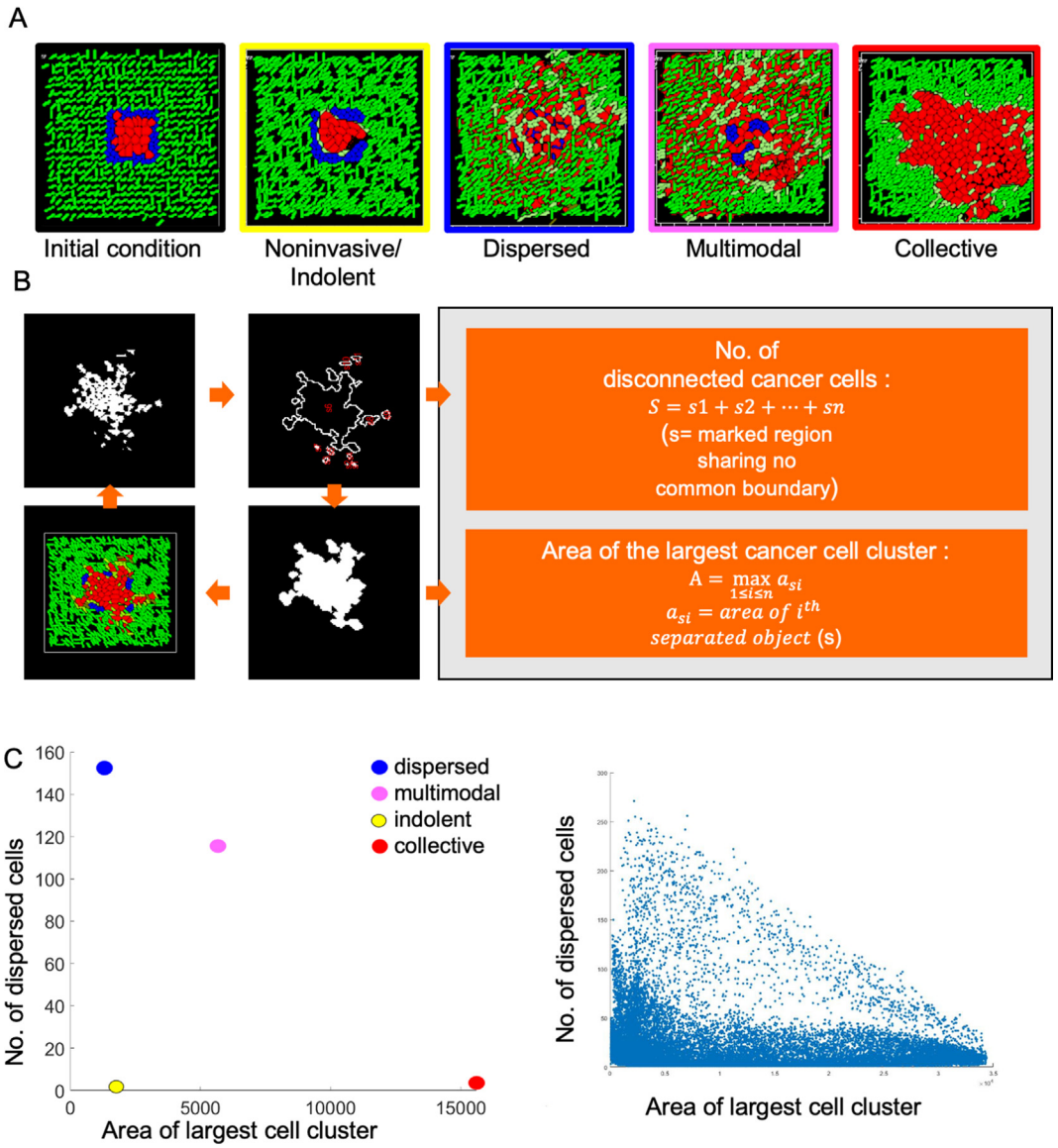

Fig. 2. Representation of invasion and construction of its phenotypic space (A) Control simulations: Four simulations (red = transformed cancer cells, green = Coll I, blue = Basement membrane (BM)) represent control runs showing morphological variations with certain input variable values. In terms of invasiveness, they are characterized as **dispersed invasion** (blue), **collective invasion** (red), **multimodal invasion** (magenta) and **indolent or non-invasive phenotype** (yellow). (B) Depiction of computation of the invasion outputs: MATLAB® is used to quantify the morphology of the cancer cell mass in the simulations. 1. Images of all simulations are collected at the 1500th Monte Carlo step (MCS). 2. The images are binarized to isolate the cancer cells. 3. All dispersed 'objects' (the objects share no common boundary with each other) are identified and counted and is called 'No. of dispersed objects'. 4. the mass having largest total covered area is isolated and the value of that highest area is called 'Area of Largest cell cluster'. (C) (left) The invasiveness of the controls interpreted through the 2 outputs show in 1A allows the construction of a phenotypic space with X axis measuring the 'Area of largest cell cluster' and Y axis measuring the 'No. of dispersed objects'. Control simulations can therefore be mapped onto the phenotypic space of possible output points within the phenotypic space through various combinations of inputs deployed through simulations run till a similar endpoint (MCS:1500). (Right) Distribution within the phenotypic space of phenotype outputs as a result of combination of five values for each of the six inputs mentioned in (1A) and run three times (replicates). The total number of simulations originating from this combination is 5^6X3 = 46875.

based on design space hypercube (as done by (Ozik et al., 2019)), it allowed us to examine simultaneously two model outputs simultaneously, which could describe the predominant cell invasion phenotypes.

2.2. Identification of optimal clustering of the invasive phenotypic space

We next investigated the optimal number of phenotypic clusters that can best classify the scatter of outputs in the two-dimensional phenotypic space. Such approaches are commonly used for gene expression studies to unravel hidden patterns in multi-variable high-dimensional spaces (Oyelade et al., 2016). K-means algorithm is a commonly used unsupervised clustering method which, given *a priori* an integer value of K, partitions the given dataset into K disjoint subsets (Macqueen, 1967). The selection of a random initial seed point for each of a preferred number of clusters is used to cluster the remaining data points; thus, different runs of K-means could possibly give rise to distinct clusters and their arrangements.

We performed K-means clustering on the invasion phenotypic space for K = 2 to K = 10 for multiple instances and examined cluster patterns across multiple (n = 15) runs for every value of K (Fig. 3 and Supplementary Fig. 2). The variation in clustering patterns was lowest for K = 2–5 (2 patterns, with one pattern predominating in frequency of appearance) and increased for values of K > 5.

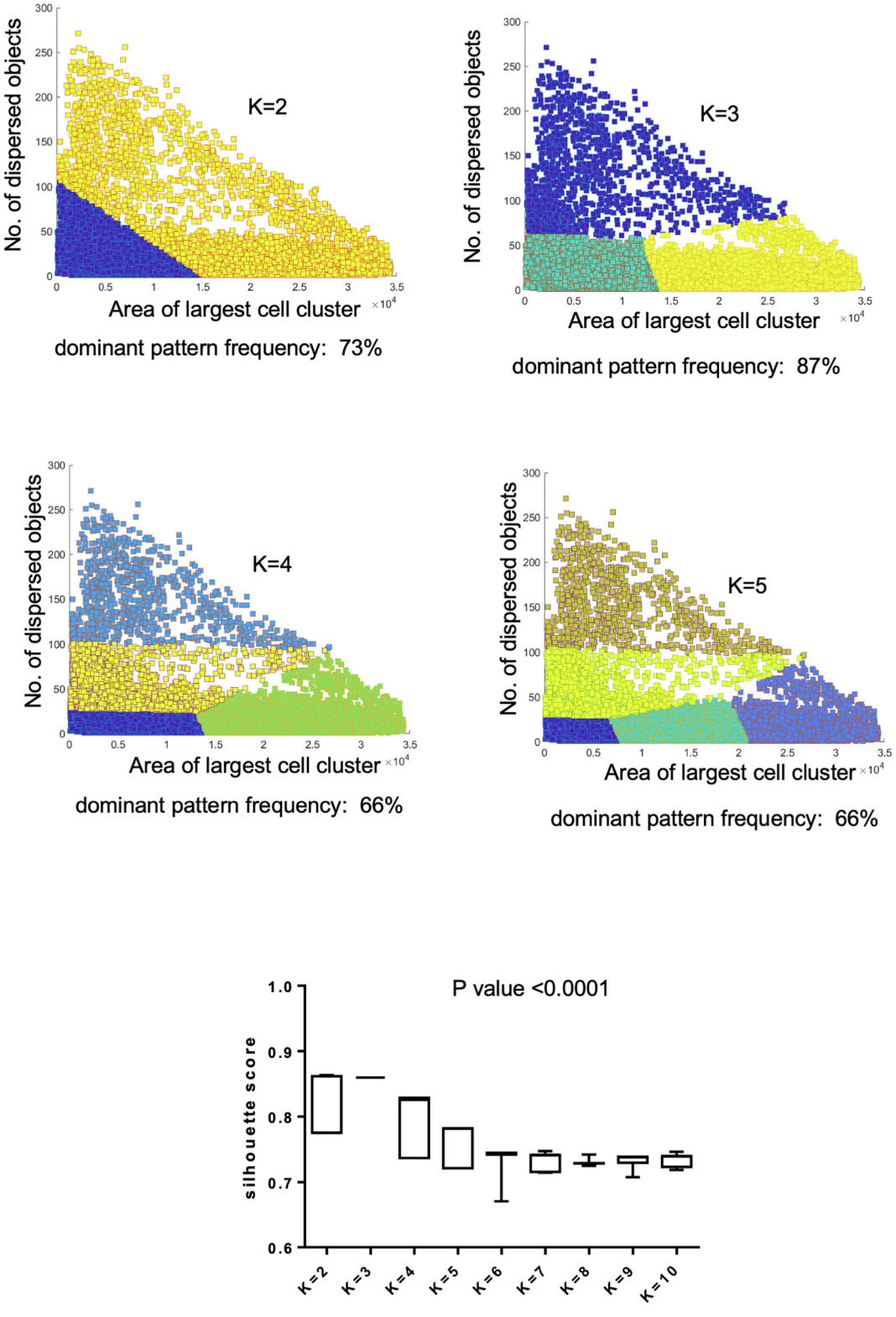

Fig. 3. The invasion phenotypic outputs can be optimally segregated into five clusters All the simulation outputs in the phenotypic space (in Fig. 1D) are analyzed with K-means clustering using cluster number K = 2–5 (top). Clustering was performed 15 times with random initial cluster centers. The dominant cluster phenotype patterns are shown along with their proportional representation within the 15 replicates. (Cluster patterns for K = 5–10 shown in supplementary Fig. 2). The optimal value for K computed using the Silhouette method are computed for K = 2–10 with X axis signifying silhouette values and Y axis representing cluster numbers. Box-and-whisker plots for silhouette values across 15 clustering replicates in different K-value groups are plotted in the box and whisker plot (bottom). Statistical test was performed using unpaired ANOVA with Tukey's post hoc multiple comparison ($p < 0.0001$) (Supplementary File 1).

Next, we computed Silhouette scores on the K-means to quantify the consistency in clustering, for varied values of K. Silhouette scores are indications of how similar a data-point is to others in its own clusters, compared to those in other clusters. Thus, Silhouette scores provide a measure of both the tightness of the clusters defined as well as the extent of separation among them. These val-

ues range from −1 to + 1; the higher the value, the closer a given datapoint is to other points in those clusters and the farther it is from other clusters (Zhao et al., 2018). Thus, a higher average score would indicate a greater degree of cluster separation. The silhouette scores for K = 2–5 showed high scores with a peak at K = 3. In comparison, lower scores were obtained for cluster patterns with K > 5 (Fig. 3 and Supplementary Fig. 2). Moreover, the mean scores for K > 5 clusters plateaued with insignificant difference with respect to each other (Supplementary File 1).

2.3. Distinct phenotypic morphologies were observed for K = 5 cluster pattern

Having performed the K-means clustering, we examined the phenotypes subsumed within the individual clusters for cellular patterns corresponding to histopathological signatures seen in breast cancer. We chose representative outputs within each cluster (in the middle of a cluster, near its boundary with the other cluster or close to the X/Y axis) and examined the endpoint of simulation (1500th Monte Carlo Step (MCS) of the simulations). The outputs belonging to the two clusters of the dominant K = 2 pattern, were prognostic of indolent/non-invasive and invasive phenotypes (Supplementary Fig. 3 left). Similarly, an examination of the phenotypic morphologies characteristic of the clusters in the dominant K = 3 pattern suggested indolent/non-invasive, coarse-grained- dispersed, and -collective modes (outputs closer to X and Y axis showed the more classical invasive morphologies, whereas those closer to X = Y showed migratory modes that were mixtures of both dispersed and collective invasion) (Supplementary Fig. 3 middle). The dominant K = 4 cluster pattern was a modification of the K = 3 pattern, with the latter's coarse-grained dispersed invasion-comprising cluster fragmenting into a more classical dispersed migration phenotype-containing cluster and another that comprised the multimodal morphology (Supplementary Fig. 3 right). The dominant K = 5 cluster pattern retained the distinct clusters of its K = 4 counterpart with one exception: the fifth cluster represented a portion of the collective cluster that exhibited interdigitating migratory phenotypes, prognostic of papillary cancers. Cellular streams of such morphologies are reminiscent of fingering instabilities seen for immiscible fluids of distinct densities (Aref and Tryggvason, 1989; Mikaelian, 1990) (Fig. 4). The remnant collective cluster portion consisted of phenotypes that display cells migrating outward-radially as a bulk. For K > 5, little difference in phenotypes could be visually appreciated between the new clusters that appeared and segmented the older ones.

Our study concurs with previous experimental examinations of cancer cell phenotypes in 3D, wherein cell lines within BM matrices exhibited mass-, grape- or stellate morphologies (Kenny et al., 2007). However, the addition of a collagen-like fibrillar ECM in our computational model unmasks stunning phenotypic diversity within the stellate morphology through an operational dialectic between cellular connectedness and dispersal.

We sought to investigate if the outputs within what we labelled as the noninvasive or indolent cluster indeed showed lower dissemination relative to the invasive modes. To confirm this, we mapped the area of the smallest circle that could enclose all the cells for a given output within the phenotypic space. The mean invasion in the bulk collective invasive cluster was highest followed by the dispersed invasive cluster, multimodal and papillary invasive clusters; the indolent cluster indeed invaded very poorly with respect to the other four (Supplementary Fig. 4).

In order to investigate whether the morphological end-point phenotypes of our simulations were the result of an interplay of migration and proliferation, we examined snapshots of the intermediate stages of the simulations. In all cases: dispersed, collective and multimodal, the diverse invasive morphologies came about through the cells dividing and moving in a outwardly radial manner (Fig. 5). To further confirm the role of migration in the phenotypes that we observed, we performed the simulations by minimizing the adhesion of cells to ECM, which is crucial for

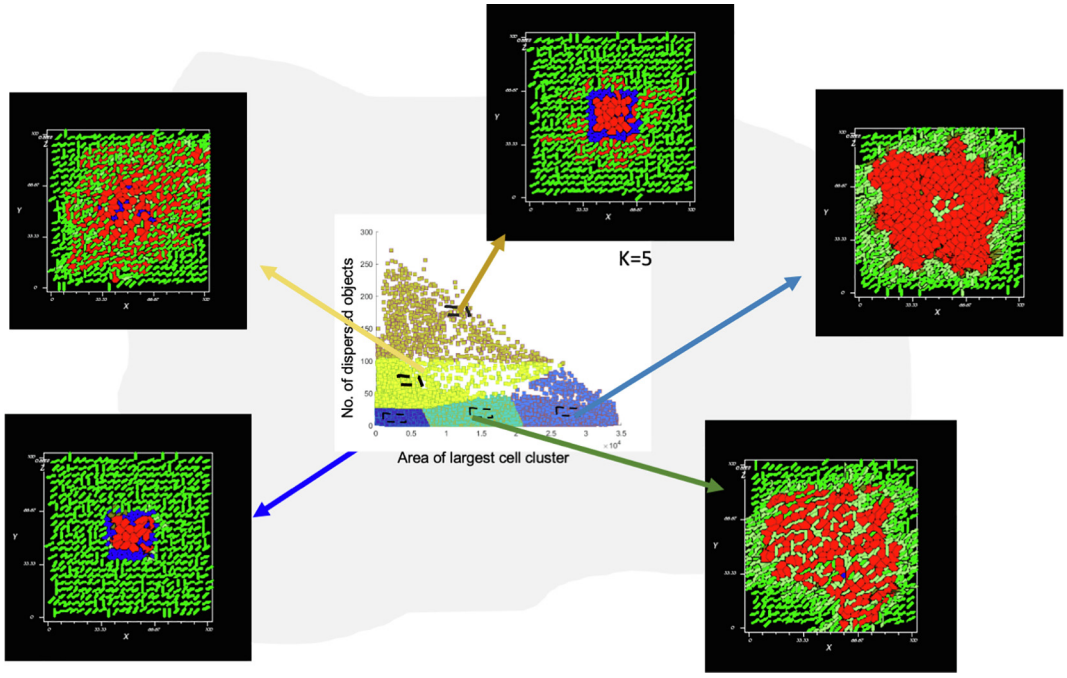

Fig. 4. Visualization of distinct invasive phenotypes across the phenotypic space The simulation images representing invasion morphologies at MCS 1500 are mapped to their respective cluster within a (K = 5)-means clustered phenotypic space in the middle. The end point of a simulation output chosen within the indolent/non-invasive cluster (dark blue) close to the X = 0, Y = 0 shows scarce invasion of cells from the originating locus. The end point of simulation for the papillary collective invasion cluster (green) shows digitating masses of cells. The end point of simulation for the bulk collective invasion cluster (light blue) shows a radially progressing mass of cells. The end point of simulation for the multimodal invasion cluster (yellow) shows a central bulk of cells surrounded by dispersed cells and cellular clusters. The end point of simulation for the dispersed invasion cluster (mustard yellow)) shows a predominantly dispersed population of single cells.

matrix mesenchymal migration, and in the case of bulk collective invasion, by decreasing the relative MMP threshold required for ECM proteolysis (Supplementary Fig. 5). Impairment of migratory abilities abrogated invasion, highlighting the requirement of migration for ECM invasion.

2.4. Each cluster shows distinct input signatures

We next asked which of the inputs (Fig. 1A) may be proportionately greater represented within each of the five clusters. In order to do so, we estimated the proportion of outputs within each cluster associated with the lowest and highest values of each input. To our pleasant surprise, each cluster displayed a unique combination of extreme input value proportion.

2.4.1. Dispersed invasion is specified by high cell-ECM adhesion and low cell–cell adhesion

All the outputs within the cluster for dispersed invasion were associated with the highest value for cell-Coll I adhesion (Table 1). >33% outputs were associated with highest levels of cell-BM adhesion and lowest levels of cell–cell adhesion (Table 1). Interestingly, none of the output clusters were associated with either the highest

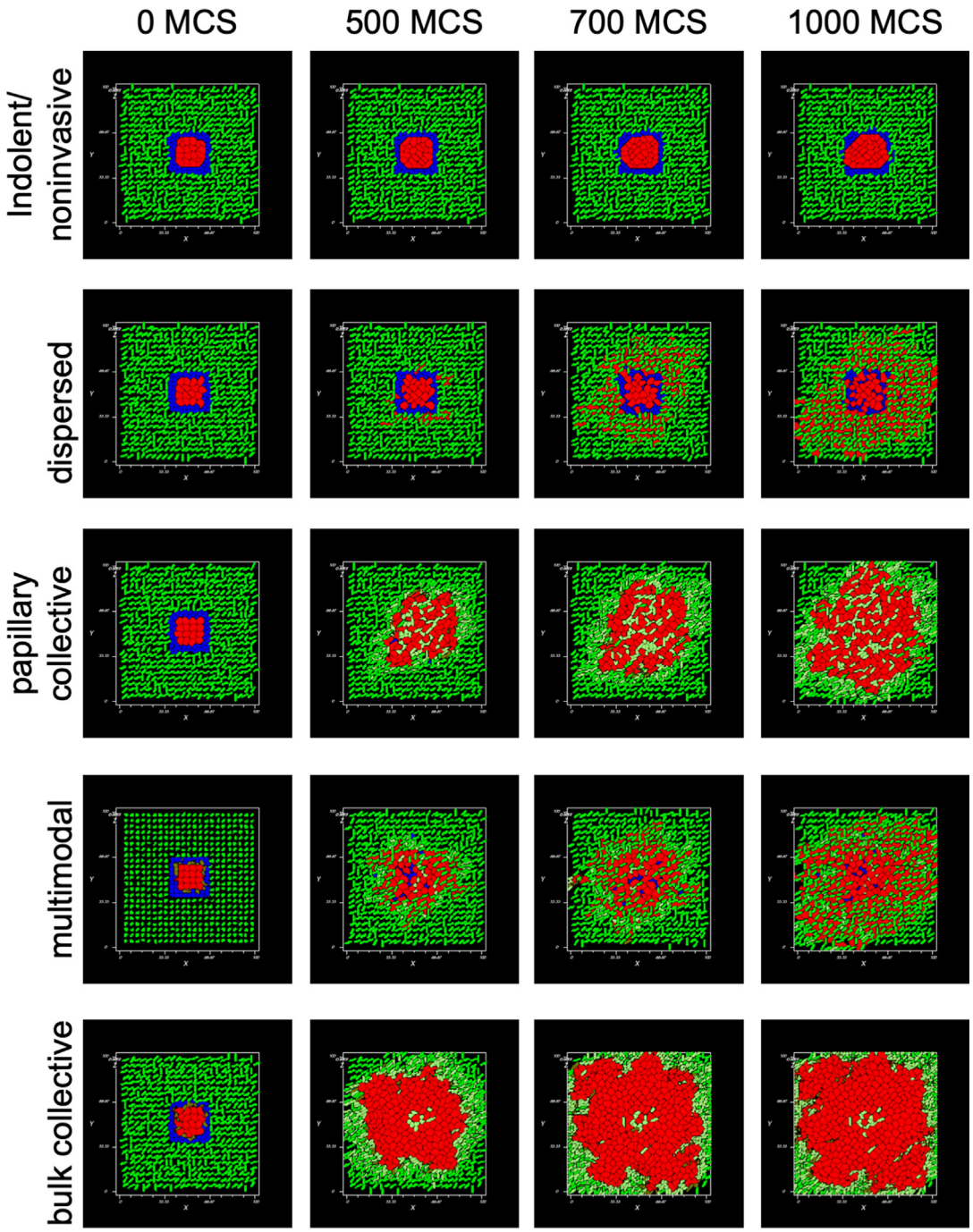

Fig. 5. Temporal Progression in simulation of different invasion modes Images from MCS 0 (leftmost), 500 (second from left) 700 (second from right), and 1000 (rightmost) of representative simulations of the same initial core of cells surrounded by ECM, showing the inability for invasion (top row), dispersed invasion (2nd row from top), papillary collective invasion (3rd row from top), multimodal invasion (2nd row from bottom) and bulk collective invasion (1st row from bottom). Cells are depicted in red, BM in blue and Coll I in green.

or lowest rates of MMP diffusion. Decreasing the ECM adhesion values for these outputs resulted in transition of a predominant proportion of the outputs (we highlight proportions for the present and following sections as =>50% of outputs, unless mentioned otherwise) to the indolent/noninvasive cluster (Fig. 6). Maximizing the low values of cell–cell adhesion resulted in output transitions to both the indolent/non-invasive and multimodal cluster (Supplementary Fig. 6).

These observations are consistent with experiments wherein mesenchymal breast cancer cells (with minimal cell–cell adhesion) are clustered and cultivated within BM- and collagen-rich ECMs: greater dispersed invasion is congruent with higher epithelial adhesion to both matrices (Pally et al., 2021).

2.4.2. Bulk collective invasion is strongly dependent on proliferation and ECM proteolysis

Outputs that represent bulk invasion with cells migrating radially outward were predominantly associated with the highest values of cell proliferation, high cell-Coll I adhesion, and high MMP diffusion rates (Table 1). Minimization of both proliferation and MMP diffusion rate transitioned most of the outputs to the indolent/non-invasive cluster (Fig. 7). Interestingly, minimizing cell-Coll I adhesion transitioned a proportion of the outputs to the indolent/noninvasive and papillary invasion cluster (Supplementary Fig. 6 middle). In consonance with recent publications suggesting an ambivalent role for cell–cell adhesion in migration through dense ECM (i.e., that collective invasion occurs in weakly adherent cells, which migrate in a polar fashion or within confined matrix milieu) (Ilina et al., 2020; Jain et al., 2020), we did not see an explicit requirement for high values of cell–cell adhesion within the collective invasion cluster.

2.4.3. Papillary collective invasion is sensitive to cell-BM adhesion and proliferation

When outputs cognate to the papillary invasion clusters were examined for input signatures, a predominant proportion showed highest values of cell proliferation (38%), cell-BM adhesion (36%), and lowest values of cooperativity between MMP and TIMP (40%) (Table 1). Upon reversal of proliferation, most of the outputs were found to transit to the indolent/noninvasive cluster (Fig. 8). Clear transitions were also observed upon altering values for cell-BM adhesion: maximization resulted in transitions of outputs to the bulk invasion cluster whereas minimization resulted in transition to the indolent/noninvasive cluster (Fig. 8). In fact, such trends were observed albeit to a lower extent upon perturbation of other inputs such as cell-Coll I adhesion and MMP diffusion rate (for which both highest (39%) and lowest values (30%) were well-represented (Supplementary Fig. 7). Increasing cooperativity resulted in transitions to indolent/noninvasive cluster and paradoxically, the bulk invasion cluster (Supplementary Fig. 6) These

Table 1
Cluster-wise apportioning of highest and lowest input values Table showing the proportion of highest and lowest values of each of 6 inputs for five states, indolent/non-invasive, dispersed, multimodal, papillary- and bulk- collective.

invasion type	cluster output frequency	**1/MMP-TIMP cooperativity**	cell proliferation	cell-Coll I contact energy	cell–cell contact energy	cell-BM contact energy	MMP diffusion rate
indolent/non-invasive	lowest value	20%	27%	12%	22%	15%	19%
	highest value	18%	13%	22%	16%	22%	7%
multimodal	lowest value	21%	8%	58%	6%	23%	6%
	highest value	15%	10%	8%	31%	15%	47%
papillary collective	lowest value	13%	0%	15%	17%	36%	30%
	highest value	40%	38%	15%	23%	13%	39%
bulk collective	lowest value	22%	0%	31%	14%	26%	22%
	highest value	15%	47%	16%	27%	16%	68%
dispersed invasion	lowest value	22%	0%	100%	3%	37%	0%
	highest value	14%	22%	0%	40%	5%	0%

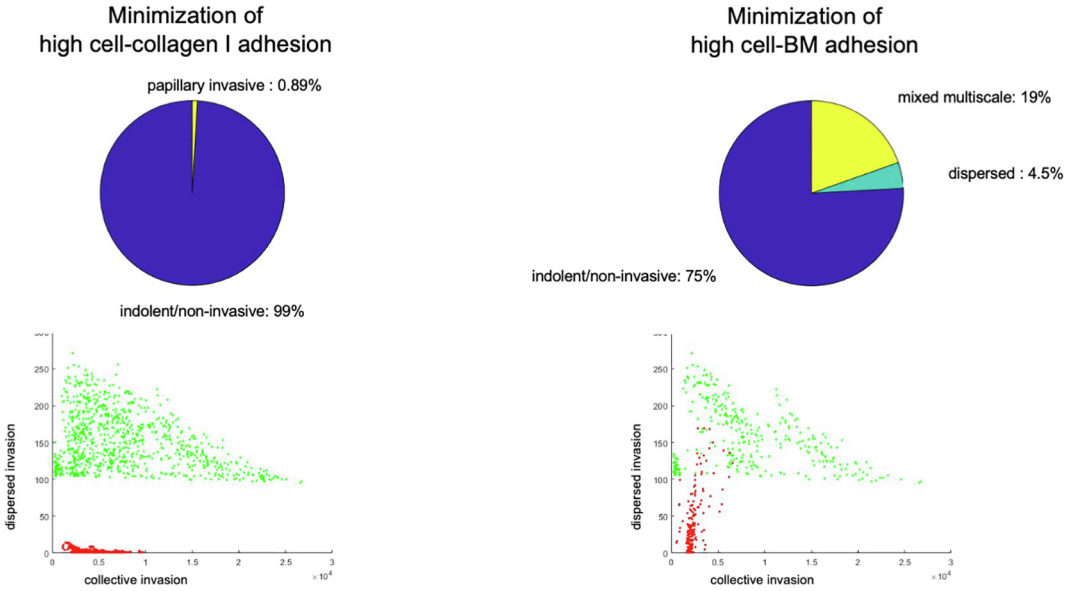

Fig. 6. Transition of outputs characteristic to the dispersed invasion cluster. Pie charts showing percentage of transitions (top) and phenotypic space (bottom) showing the initial (green) and final (red) spatial maps of the outputs from the dispersed invasion cluster upon minimization of cell-Coll I adhesion (left) and cell-BM adhesion (right).

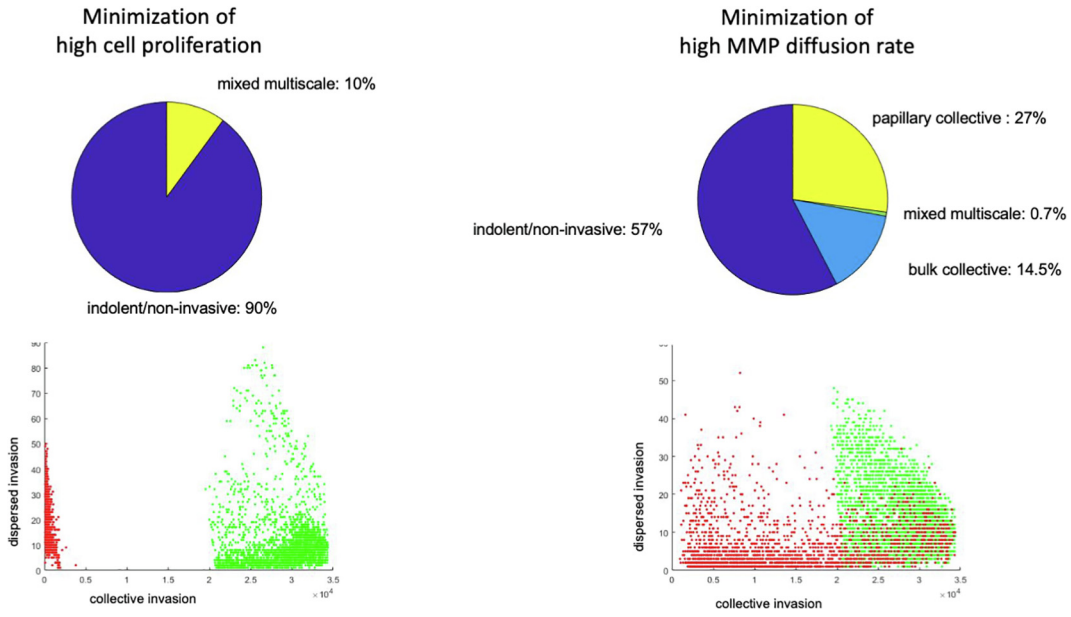

Fig. 7. Transition of outputs characteristic to the bulk collective invasion cluster. Pie charts showing percentage of transitions (top) and phenotypic space (bottom) showing the initial (green) and final (red) spatial maps of the outputs from the bulk collective invasion cluster upon minimization of cell proliferation (left) and MMP diffusion rate (right).

results suggest that the papillary cluster is more sensitive to input perturbations than other clusters.

2.4.4. Multimodal invasion is sensitive to adhesion and proteolysis

A considerable proportion of the outputs within the multimodal cluster was associated with lower intercellular adhesion (31%) greater adhesion of cells to Coll I (58%) and high MMP diffusion rate (47%) (Table 1). Minimization of the latter, and ECM adhesion resulted in the transition of a majority of outputs to the indolent/non-invasive cluster (Fig. 9). A similar transition was also observed upon increasing intercellular adhesion (Fig. 9). Similar to the dispersed invasion cluster, multimodal invasion was dependent on cell-Coll I and cell–cell adhesion. Decreasing the adhesion of cells to ECM had a similar effect as dispersed invasion outputs although much milder in extent. On the other hand, decreasing intercellular adhesion had a stronger consequence of decreasing invasion altogether for most outputs. On the other hand, it shared its dependence on high MMP diffusion rate with the bulk collective invasion cluster indicating the multimodal invasion has mechanistic underpinnings that overlap partially with the dispersed and bulk collective modes.

3. Discussion

In an illustrative review, Friedl and coworkers provided an elegant classification of generic cell invasion: they enumerated numerous movements with solitary and bulk movements at the two ends of the phenotypic spectrum (Friedl et al., 2012). Our manuscript seeks to build on this idea by subjecting it to mathematical rigor and identify its underlying assumptions and mechanisms. While Friedl and others have that distinct modes may concur spatially, their tuning model would attribute such co-occurrence to the heterogeneity in microenvironmental cues (Clark and Vignjevic, 2015). However, does the co-occurrence of dispersed and collective modes of invasion (multimodal invasion) represent a distinct invasive mode, wrought through distinct signatures from a tunable combination of inputs? In this manuscript, we argue that such is the case. In fact, we identify four categories of invasion (along with an indolent/non-invasive category) that have partially overlapping input contributions.

Invasion of cancer cells has been characterized as non-equilibrium phase separation of mesoscale multicellular aggregates (Yang et al., 2019). This idea is an extension of previous frameworks which describe spreading cellular ensembles as liquids and dispersed cells as 2D gases (Sadati et al., 2013; Trepat and Fredberg, 2011). Jammed non-invasive states have been likened to ‘solid phases’ and the transitions between non-invasive and invasive (collective and dispersed) phenotypes can be compared with phase transition dynamics. The novelty of our contribution within this framework stems from the crucial addition of two ECM microenvironments instead of one as well as the recreation of the collagenous ECM by invading cancer cells. This is not to add needlessly to the complexity but to incorporate essential characteristics of tumorigenic epithelial tissues (Naba et al., 2014; Nelson and Bissell, 2005). The production of fresh collagenous ECM is being increasingly demonstrated to play a crucial role in defining the invasive behavior of cancers. The ECM secreted by cancers is rich in fibrillar collagen. In a recent preprint, we identify unique physicochemical features associated with the collagenous ECM secreted by invasive breast cancer cells (Dasgupta et al., 2020). Such observations have been corroborated in several cancers including that of breast (Naba et al., 2014). Upon incorporation of these two features, we observe that the phenotypic distribution that is intermediate between pure collective and dispersed states can be fundamentally split into two clusters, with specific input contributions. Our findings allow us to extend the characterization of mesoscale multicellular phenotypes based on soft matter models (Gonzalez-Rodriguez et al., 2012), as gaseous (dispersed invasion) solid (indolent/non-invasive), liquid (papillary collective) and possibly polydisperse (multimodal).

Surgical histopathological literature is replete with observations of multimodal behavior in cancer invasion. In the context of colorectal carcinoma, Prall and coworkers have made meticulous observations on ‘tumor budding’, wherein single cells or small collectives of tumor cells escape from growing edges of malignant

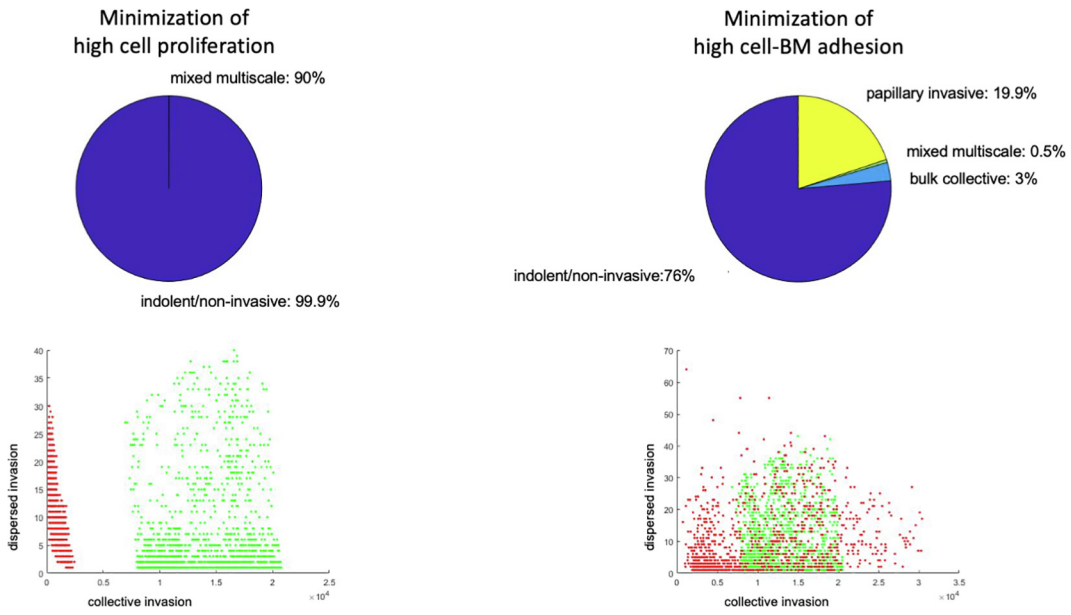

Fig. 8. Transition of outputs characteristic to the papillary collective invasion cluster. Pie charts showing percentage of transitions (top) and phenotypic space (bottom) showing the initial (green) and final (red) spatial maps of the outputs from the papillary collective invasion cluster upon minimization of cell proliferation (left) and cell-BM adhesion (right).

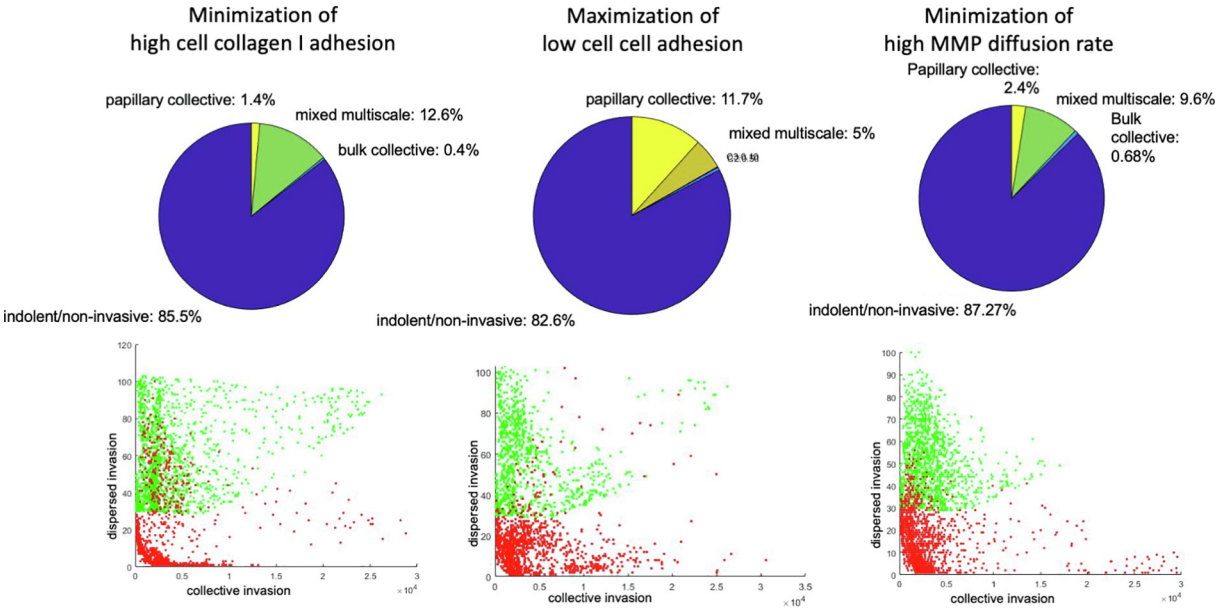

Fig. 9. Transition of outputs characteristic to the multimodal invasion cluster. Pie charts showing percentage of transitions (top) and phenotypic space (bottom) showing the initial (green) and final (red) spatial maps of the outputs from the multimodal invasion cluster upon minimization of cell-Coll I adhesion (left), maximization of cell–cell adhesion (middle) and minimization of MMP diffusion rate (right).

neoplasms (Prall et al., 2005, 2009). Such multimodal behavior is associated with a more sinister kinetics of metastasis and poor prognosis (Hase et al., 1993; Prall et al., 2005; Prall and Ostwald, 2007). Tumor budding has been observed in breast and pancreatic cancers as well (Petrova et al., 2019; Salhia et al., 2015) and have been connected to a partial EMT phenotype (Bronsert et al., 2014; Grigore et al., 2016). Our previously published experiments, which were crucial to the development of the computational model we have explored here, described multimodal invasion, which is phenomenologically similar to tumor budding (Pally et al., 2019). Indeed, early investigations by others confirm our empirical and theoretical findings that surface proteins and ECM play key roles contributing to multimodal invasion (Graves et al., 2016; Masaki et al., 2003). Contemporary literature on cancer invasion indicates that collective invasion may potentiate metastasis further than single cell dispersed invasion. Our model confirms this (Supplementary Fig. 4) but goes beyond these observations in contextualizing collective invasion as not one type but three, with distinct mechanistic bases, plasticity and invasiveness. Our observations thus add to the burdgeoning literature on the mechanistic understanding of intra- and intertumoral heterogeneity.

A close examination of the input value representations between the distinct clusters permitted within our models suggests that dispersed- and multimodal invasion are both characterized by

higher adhesion of cells to Coll I and lower adhesion to each other. Both processes do not depend on high cellular proliferation for their progress. However, dispersed invasion seems agnostic to ECM degradation, multimodal invasion is characterized by a greater MMP diffusion rate. Papillary and bulk collective invasion cluster outputs are both characterized by high cellular proliferation. Therein, their similarity ends: bulk collective invasion outputs are predominantly dependent on high Coll I adhesion and high MMP diffusion rates, whereas the papillary invasion cluster houses outputs with a dependence on cell-BM adhesion and low MMP-TIMP cooperativity for ECM degradation. Interestingly, it is the cooperativity between MMP and TIMP for degradation that dominates within the bulk invasion cluster, which upon minimization allows the outputs to transit to the papillary invasion cluster, indicating how degradation molds the shape of the invading cellular collectives. Our model also predicts that differential adhesivity to distinct ECMs may determine the morphology of collective invasion. Indeed, slenderer finger-like projections of migrating cellular collectives are observed when invasive breast cancer cells are cultivated only in laminin-rich basement membrane matrices (referred to as the stellate morphology), which is consistent with our prediction for papillary invasion. Schematic depictions of the distinct phenomenological enrichment for each cluster in our analysis is shown in Fig. 10 (top). The mechanistic underpinnings of major and minor cluster transitions are schematically depicted in Fig. 10 (bottom) and Supplementary Fig. 8, respectively.

At this point of time, our study does not incorporate three salient aspects of invading cancer cells. The first is the change in shape of cells as they move through matrix microenvironments. This distinguishes amoeboid from mesenchymal single cell migration and is associated with shape-based asymmetries in remodeling of ECM intercellular adhesion (Paňková et al., 2010). Despite this, as well as the fact that we do not incorporate any subcellular features associated with migration, such as polarized actin turnover and the role of small GTPases like Rho/Rac (Ridley, 2015), we believe our dispersed invasion is mesenchymal in nature as it is predicated on adhesion of cells to the ECM (which distinguishes it from amoeboid migration).. However, cell shape dynamics will be implemented in our future efforts. Secondly, our computational environment does not incorporate the stromal cells that contribute in significant ways to the phenomenology of cancer cell invasion (Labernadie et al., 2017) due to limitations of the sheer computational power required to compute the dynamics of a multi-cell multi-ECM environment. We assume that the R-D dynamics of MMP-TIMP incorporated in the computational environment is a downstream effect of the cancer and stromal cell activities. This assumption will be tested in future efforts. Last, but not the least, our model does not incorporate cell polarity which has been proposed to contribute to active models of soft biological matter

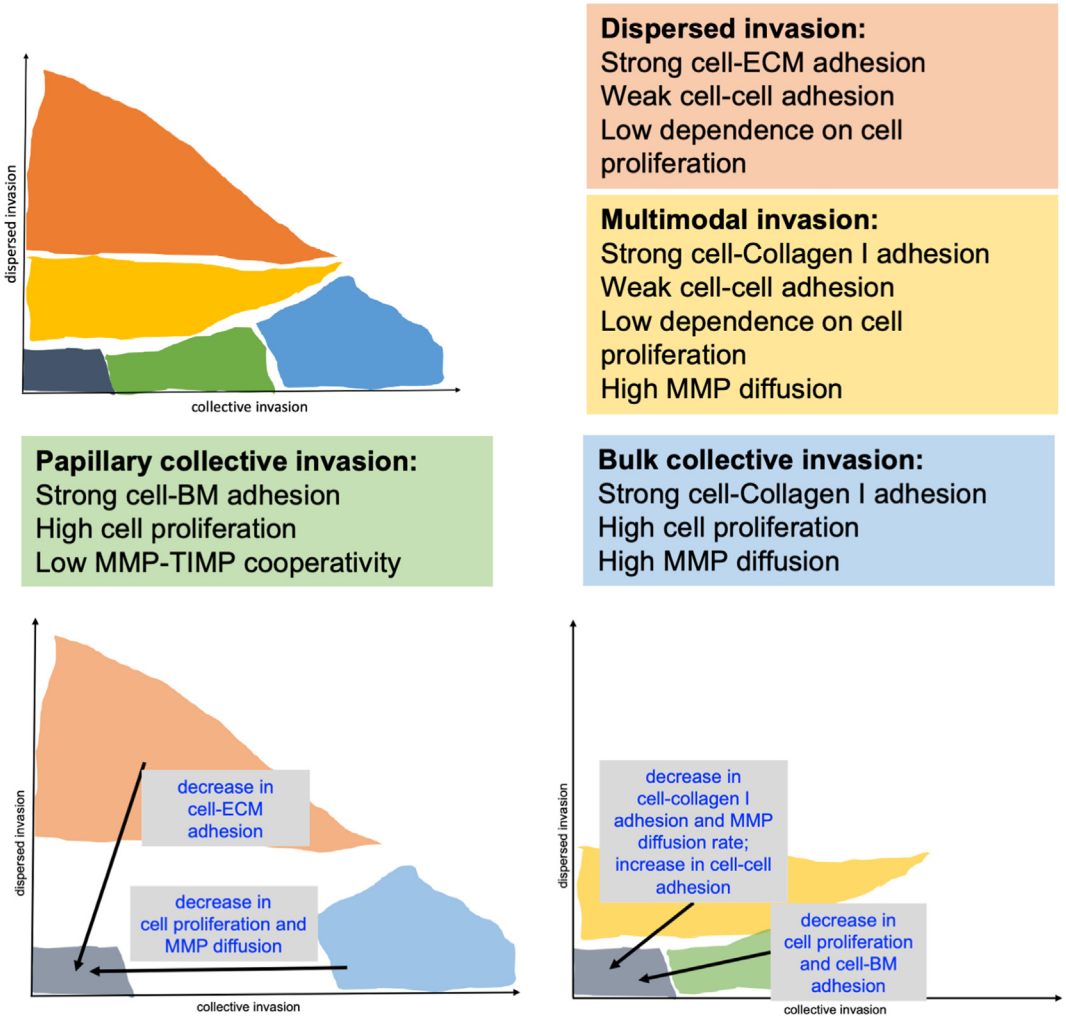

Fig. 10. (Top) Schematic depiction of invasive states and the canonical contributions of phenomenological inputs to each state. (Bottom) Schematic depiction of the major transitions between outputs of specific cluster pairs upon reversing the highest or lowest values of specific inputs.

(Pérez-González et al., 2019) and predict migration in the absence of proliferation (Tlili et al., 2018). Future efforts will be devoted to computational investigating the properties of polarized polydisperse states. At present though, our effort serves to put multimodal migratory behavior in the fundamental center of the concept of cancer invasion. Understanding the process has potentially far-reaching consequences for future therapeutic efforts.

We would conclude by drawing a parallel between our study and the modeling efforts employed for investigating developmental processes (Alber et al., 2006, 2004; Christley et al., 2007; Harrison et al., 2011; Izaguirre et al., 2004; Kiskowski et al., 2004; Merks and Glazier, 2006). While our model derives its motivation, initial conditions and tissue geometry (which have been shown to be a crucial determinant in morphogenetic pattern formation (Nelson et al., 2006)) from breast cancerous contexts (Bhat and Bissell, 2014), one can as well interpret our model as a developmental system wherein inter-agent adhesion and reaction–diffusion based phenomena sculpt cellular patterns. In fact, several of our model inputs represent the biological physics associated with the framework of dynamical patterning modules, which has been employed to study the evolution and logic of developmental mechanisms (Newman and Bhat, 2008, 2009). In effect, this suggests that the redeployment of developmental and morphogenetic principles in the context of genomic aberrations may underlie the mechanisms behind discrete invasive behaviors of cancer cells and the transitions between them.

3.1. Modelling framework

Compucell3D (CC3D) is a problem-solving environment that combines the lattice-based GGH (Glazier–Graner–Hogeweg) model or CPM (Cellular Potts model) with PDE solvers and other models to allow for study and simulation of multiscale virtual biological and non-biological processes such as foam dynamics (Swat et al., 2012). The software divides the whole simulation lattice into 'cells' (collection of pixels). A specific 'cell type' is assigned to each of them. Interaction parameters between cell types can be made to approximate biological constraints between components, similar to that of the original in vitro or *in vivo* biological system. Such constraints or parameters regulate the simulation through the effective energy or **Hamiltonian (H)** calculated at each **Monte Carlo Step (MCS)**. Calculation of H determines the allowed configuration and behavior of cells at each MCS.

Hamiltonian or effective energy calculation at each MCS:

$$H = \sum_{\substack{i,j \\ neighbours}} J(\tau(\sigma_i),\tau(\sigma_j))(1-\delta(\sigma_i,\sigma_j)) + \sum_{\sigma}[\lambda_{vol}(\sigma)(v(\sigma)-V_t(\sigma))^2 + H_{chemo(GF)}$$

$$\Delta \boldsymbol{H}_{\boldsymbol{chemo(GF)}} = -\lambda_{\boldsymbol{chemo}}.(\boldsymbol{c_j}-\boldsymbol{c_i})$$

Index(σ)-copy attempt (from pixel i to j) success or rejection incorporating Boltzmann probability function:

For $\Delta \boldsymbol{H} \leq 0$ condition, the associated index-copy attempt will be successful, so the target pixels are updated. So, success probability is $P = 1$

For $\Delta \boldsymbol{H} > 0$ condition, the associated index-copy attempt will be successful with a probability of $P = e^{-(\frac{\Delta H}{T_m})}$ and it will be unsuccessful with a probability $P' = 1 - P$

There are 4 contributors for calculating the H for cells.

The first contributor is the sum over all neighboring pairs of lattice sites *i* and *j* with associated contact energies (*J*) between the pair of cells indexed at those *i* and *j*. In this term, *i, j* denotes index of pixel, σ denotes cell index or ID, and τ denotes cell-type. The Dirac δ function in this term will ensure that only the $\sigma_i \neq \sigma_j$ terms are calculated (i,j belonging to same cell will not be considered). Contact energies are symmetric [$J(\tau(\sigma_i),\tau(\sigma_j)) = J(\tau(\sigma_j),\tau(\sigma_i))$] . The contact energy between two cells is considered to be inversely proportional to adhesion between those two cells.

The second contributor is a function of the volume constraint on the cell, where for the cell σ, $\lambda_{vol}(\sigma)$ denotes the *inverse compressibility* of the cell, $v(\sigma)$ is the number of pixels in the cell (*volume of the cell*), and $V_t(\sigma)$ is the cell's *target volume*. For each cell, this term is governed by its growth equation.

The third term is relevant for biased motility of the cell due to chemotaxis. For calculation of $\Delta \boldsymbol{H}_{\boldsymbol{chemo(GF)}}$, $\boldsymbol{c_j}$ represents the concentration of the chemical field ('GF' for our simulations) at index-copy target pixel (j) and $\boldsymbol{c_i}$ represents the concentration at index-copy source pixel (i). $\lambda_{\boldsymbol{chemo}}$ is a constant which determines how strongly the cell will respond to the external chemical gradient by its value and its sign determines the whether the cell should move towards positive or negative gradient of concentration.

In the Boltzmann probability function, Δ*H* represents the calculated change in overall Hamiltonian of the system between the system-configuration at previous MCS and a specific system-configuration at current MCS. T_m relates to effective membrane fluctuation for the cell.

(https://compucell3dreferencemanual.readthedocs.io/en/latest/index.html) (Swat et al., 2012).

3.1.1. Simulation lattice

We use a 100*100*1-pixel square lattice with non-periodic boundary for all the simulations (the initial configuration of simulations resembles Fig. 1(C) where no invasion of any type is observed).

3.1.2. Cell types

There are a total of 6 different cell types used in the simulations-

Medium: all cells with unassigned cell type are medium cells. These cells act as free, uninterrupted space in the simulation space, and their contact energy with cancer cells have been kept high so as to disallow interference with interactions of the latter with matrix cells.

Cancer: these cells are initially situated at the center grid surrounded by basement membrane (BM). Cancer cells start as rectangular objects of 16-unit volume (4 × 4 pixels), spanning a total 16 × 16 × 1 unit volume (16 cancer cells) at the center (*x, y* = 43:57) of the simulation grid without any intercellular space. Cancer is the only cell type that is allowed to grow and proliferate. To differentiate from non-cellular components, cancer cells have membrane fluctuation unlike others.

BM (laminin): This cell type surrounds the cancer cells in the initial configuration. 2 layers of tightly packed BM cells (x, y = 37:63; 3 × 3 pixels = 9 unit volume) separate the cancer cells from C1 cells. To approximate extracellular matrix (ECM) architecture surrounding luminal epithelial cells in mammary duct, BM cells are modelled as dense adhesive bloblike objects to mimic the lamina densa of basal lamina.

(Collagen) C1: Outside BM cells, fibrillar C1 cells mimics the interconnected fibrils of collagen I. C1 cells span the remaining space of the simulation lattice (x, y = 63:100). Interfibrillar gaps are characteristic of the C1 cell region unlike BM. The gaps aid in non-proteolytic cancer cell motility through C1 layer. In the initial configuration of the simulation, elongated C1 cells are orientated in random directions with each cellshaving 4 × 2 = 8 unit volume.

C_lysed: This cell type is used in an intermediate step during matrix degradation and regeneration. Reaction-diffusion dynamics of the chemicals secreted by cancer cells allows for degradation of

BM and C1 matrix cells. Upon meeting certain criteria for degradation, the BM or C1 cell type of a particular cell becomes C_lysed, although retaining the shape and size of that cell. These cells track the MCS from their individual degradation event and transform into newly synthesized matrix cells after 20 MCS. They have properties specified as intermediates of C1 and medium cell types. C-lysed type signifies the degraded ECM, predominantly Coll I fibers. Collagen fibers upon degradation are known to produce substrates that act as attractant cues for chemotaxis (Postlethwaite et al., 1978). In addition, collagenous matrices have been shown to be depots of growth factors (Schuppan et al., 1998; Somasundaram et al., 2002, 2000).

NC1: Designed to mimic the 'cancer matrisome', the newly synthesized matrix cells are denoted as NC1. These cells are almost like C1 in their behavior and can undergo further degradation to become C_lysed and subsequently after 20 MCS, would become NC1 again. If unremodeled by cancer cells, the C_lysed and NC1 cell type transformations keep their position, size and shape unchanged.

The exact difference between C1 (stromal collagen) and NC1 (newly synthesized collagen) are as follows:

1. There is a volume reduction we have implemented in NC1, to account for diffusion of soluble degraded ECM, 0.005 unit vol./MCS * 20 MCS = 0.1unit
2. The chemoattractant GF is secreted by C1, when it comes in contact with C_Lysed i.e., during degradation. But even though NC1 can be degraded, it does not secrete GF. Both of them get converted into C_Lysed and that cell-type secretes GF.
3. Among both, only the contact energy term between cell and C1 is an input variable for parameter scan. The interaction between the components of our model is depicted schematically in Fig. 1B.

3.1.3. Contact energies

As the whole simulation lattice is divided into cells, the contact energy is used to regulate the sorting of all the cells. Specific contact energy values are assigned to all pairs of interactions between different and same cell types. The contact energy is also *inversely proportional* to adhesion between the respective cell type pair or components of the system. As there are a total of 6 cell types in the simulation, there are total 21 contact energies that need to be assigned and the values determine the differential adhesion. The values of the contact energies were set using control and validation experiments from literature (Pally et al., 2019; Swat et al., 2012). 3 among those 21 contact energy- or adhesion- parameters were selected as input variables, which would be changed during further analysis. These 3 contact energies or adhesions are associated with pairs of cell types of only cancer cells (**c-c CE**), cancer cells and BM (**c-lam CE**), cancer cells and C1 (**c-c1 CE**) since in our previous efforts we had identified the combination of other contact energies (such as those between BM and Coll I that were permissive for invasion-based simulations.

The neighbourhood ('NeighborOrder') for adhesion term is 2. This ensures for a square shaped cell, all neighbouring cells on its 4 sides along with cells on the 4 corners are considered during the Hamiltonian calculation.

3.1.4. Reaction diffusion

CC3D allows chemical fields to determine specific spatiotemporal cellular behavior during simulation. The fields contain the values of concentration of the chemical at each location of the simulation grid. Two chemicals, A and I, are used as activator and its inhibitor as per reaction diffusion dynamics and their concentrations are governed by the partial differential equations (PDE). The governing equations for these two fields are:

$$\frac{\partial[A]}{\partial t} = D_A \nabla^2[A] + a - \delta_A[A] \quad (1)$$

$$\frac{\partial[I]}{\partial t} = D_I \nabla^2[I] + b - \delta_I[I] \quad (2)$$

$$b = a = K - (c * [I] - d * [A]) \quad (3)$$

Where, [A], [I]: concentration values for fields A and I.
D_A,D_I : diffusion constants of A and I
δ_A ,δ_I : degradation rates of A and I
a, b : secretion rate of A and I
t ≡ MCS

Default parameterizations, D_A= input variable, D_I= 0.04, δ_A=δ_I = 0.003, K = 2.0, c = 4.0, d = 2.0

Here A is considered as the activated form of matrix metalloproteinases (MMPs) and I is considered as tissue inhibitor of matrix metalloproteinases (TIMP). The difference in diffusion constants of A and I formulates the pattern in Turing space, so altering one of them (in this case, D_A) can result in different RD dynamics for different simulations. Activation (or secretion of the activated form i.e. 'a') of A is assumed to be dependent on its inhibitors (inversely) and on its own concentration (autocatalysis). The cancer cells secrete both A and I when they come in contact with matrix cells such as C1, BM and NC1. Their concentrations are also calculated at the center of mass of the matrix cells.

'DiffusionSolverFE' is the name of the PDE solver in cc3d which was used for reaction–diffusion system. It uses Forward Euler explicit numerical scheme to solve the differential equation related to the chemical fields. The solver is called once every MCS to carry out calculations for all the chemical fields. The diffusion rate of the activator is used to determine the time scale of a simulation, so by changing the same time scale can be varied for different simulations.

If the ratio ([A]/[I]) of concentrations of A and I at the center of mass of any matrix cell is more than a threshold, then that matrix cell is degraded. The threshold value for the ratio is termed as MMP-TIMP cooperativity and is one of the input variables. The value of MMP-TIMP cooperativity signifies the inhibition effect of the inhibitor on the activator's activity (matrix degradation) during the course of a simulation. After degradation and conversion to C_lysed cell type, the cell becomes NC1 type in 10 MCS which undergoes same treatment as matrix cells again. This regeneration of matrix is essential to eliminate unnecessary free spaces formed as an artefact of matrix degradation which takes the computational model closer to its experimental counterpart. Volume of all the 'C_lysed' cell types are subjected to 0.1 unit volume decrease at each MCS to mimic dissipation of degraded matrix materials *in vivo*.

3.1.5. Growth and proliferation

Cancer cells are designed to grow in linear combination of two processes.

$$\frac{dV}{dt} = G * [g * p + [GF] * q]$$

Where V = volume of cancer cell
g = measure of nutrient availability
[GF] = concentration of growth factor (GF) at center of mass of 'CELL'
p, q = constants
G = Growth rate coefficient

The common surface area of a cancer cell with its neighboring cancer cell (k) and the total cell surface area (s) is accessed to calculate *g* in this equation as *g=(s-k)/40*. The denominator in the calculation of *g* is due to 2D nature of the simulation as a cell can be

surrounded by other cells only in XY plane and not in Z axis. The scaling of that extra cell surface area without any neighboring cells in Z axis is provided by the denominator. Another contributor of the growth function is *[GF]* which mimics the ECM-degradation dependence of growth and proliferation (Olivares et al., 2017). The 'C_lysed' cell type is programmed to secrete GF (this is also a chemoattractant for simulated cancer cells) at each of its pixel location where the diffusion constant is kept low (0.02) to localize this growth signal to areas of matrix degradation. p (=1/12) and q (=1/21) constant values are set according to the assumed weightage of the two variables in growth equation. Value of G, then determines how much the resultant growth of the cell should be. The linear combination of the two contributors is multiplied by G, this G is changes during parameter scan. Hence, G or growth rate coefficient is considered as an input variable.

Cell division is incorporated into the cancer cells by a CC3D steppable called 'MitosisSteppable' with base function 'MitosisSteppableBase'. If any cancer cell reaches a threshold volume of 30 units then that cell will be divided in random orientation. The resultant two cells will have volumes half of its predecessor with all other properties kept same as the parent cell. In this model, growth rate is directly correlated to proliferation as it determines the volume of the cell to reach threshold for cell division.

3.1.6. Chemotaxis and migration

In our current model, we incorporate chemoattraction in order to simulate an active migration of cancer cells into their surrounding "stromal" Coll I matrix. The stromal ECM, collagen has been shown to have chemoattractant properties in undegraded and degraded states (Postlethwaite et al., 1978) (O'Brien et al., 2010).

The 'Chemotaxis' plugin implements a force on the cells through the Hamiltonian towards positive gradient of the chemical field 'GF'. The 'GF' field is secreted by degraded matrix (C_Lysed) and undegraded collagen (C1). In order to ascertain local positive chemical gradient towards undegraded C1 matrix, the C1 releases the chemoattractant in slightly greater amount than its degraded counterpart C_Lysed [secretion rate: 2.5 for C1 compared to 1.0 for C_Lysed]. Only the C1, which are close to other C1 being degraded by MMP, release this GF (to simulate the ability of the collagenous matrix to act as a sink for chemoattractants that get released upon their proteolysis) as instructed in the 'SecretionSteppable'. This is coded in the cancol2Steppables.py file in the CC3D folder and 'Simulation' subfolder.

The correspondence between simulation spatiotemporal scales and the cellular migration in 3D was arrived at through a comparison of velocity of cell migrations within Coll I matrix in 3D, imaged through time lapse videomicrography with the velocity of cells in a histotypic compucell3D environment. Using estimation of the mean cell size, 1 pixel of the Compucell3D environment was computed to be = 3 uM. Using velocity comparisons, 1 MCS was computed to be = 31 secs.

3.1.7. Parameter scan

CC3D's parameter scan feature was used to explore parameter space of the input variables. All the combinations of provided values of the parameters are considered for each individual simulation.

Here are the 5 values of the 6 input variables for a parameter scan:

MMP-TIMP cooperativity: 2,4,6,8,10
MMP (A) diffusion constant: 0.005, 0.01,0.02, 0.04, 0.08
Cell-cell contact energy: 4,18, 32, 46, 60
Cell-laminin contact energy: 4,18, 32, 46, 60
Cell-C1 contact energy: 4,18, 32, 46, 60
Cell Growth (G): 0, 0.25, 0.5, 0.75, 1

3 replicates of the parameter scan were performed.

The magnitudes relating to contact energy are relative to each other therefore share a similar range. The order of magnitude for the values of contact energies as well as MMP kinetics have been adopted from previous published literature on migration from other groups (Kumar et al., 2016) (Swat et al., 2012). In initial pilot simulations, we determined the range of values for which we could observe the maximum variation in phenotypic morphologies, specific to the spatial dimensions of our simulations. Below some of the lowest values of the parameters such as for contact energies, we did not observe any invasion. Beyond the highest values as well, the morphologies were not observed to change.

MATLAB-based analysis: The MATLAB codes and their descriptions are provided in Supplementary File 2.

Codes: All the codes relating to the manuscript can be accessed through the following link: https://github.com/drjyprk/cc3d_paper_2_iisc_git

Author contributions

DP, MKJ and RB designed the simulations. DP performed the simulations. DP, MKJ, and RB analyzed the results and wrote the paper.

Declaration of Competing Interest

The authors declare that they have no known competing financial interests or personal relationships that could have appeared to influence the work reported in this paper.

Acknowledgments

This work was supported by the Wellcome Trust/DBT India Alliance Fellowship/Grant [Grant Number IA/I/17/2/503312] awarded to Ramray Bhat. He also acknowledges support from DBT [BT/PR26526/GET/119/92/2017] and SERB [ECR/2015/000280].

Appendix A. Supplementary data

Supplementary data to this article can be found online at https://doi.org/10.1016/j.jtbi.2021.110733.

References:

Aceto, N., Bardia, A., Miyamoto, D., Donaldson, M., Wittner, B., Spencer, J., Yu, M., Pely, A., Engstrom, A., Zhu, H., Brannigan, B., Kapur, R., Stott, S., Shioda, T., Ramaswamy, S., Ting, D., Lin, C., Toner, M., Haber, D., Maheswaran, S., 2014. Circulating tumor cell clusters are oligoclonal precursors of breast cancer metastasis. Cell 158 (5), 1110–1122.

Ahmadzadeh, H., Webster, M.R., Behera, R., Jimenez Valencia, A.M., Wirtz, D., Weeraratna, A.T., Shenoy, V.B., 2017. Modeling the two-way feedback between contractility and matrix realignment reveals a nonlinear mode of cancer cell invasion. PNAS 114 (9), E1617–E1626.

Alarcón, T., Byrne, H.M., Maini, P.K., 2004. Towards whole-organ modelling of tumour growth. Prog. Biophys. Mol. Biol. 85 (2-3), 451–472.

Alber, M., Chen, N., Glimm, T., Lushnikov, P.M., 2006. Multiscale dynamics of biological cells with chemotactic interactions: from a discrete stochastic model to a continuous description. Phys. Rev. E: Stat. Nonlinear Soft Matter Phys. 73 (5). https://doi.org/10.1103/PhysRevE.73.051901.

Alber, M.S., Kiskowski, M.A., Jiang, Y., 2004. Two-stage aggregate formation via streams in myxobacteria. Phys. Rev. Lett. 93 (6). https://doi.org/10.1103/PhysRevLett.93.068102.

Allena, R., Scianna, M., Preziosi, L., 2016. A Cellular Potts Model of single cell migration in presence of durotaxis. Math. Biosci. 275, 57–70.

Andasari, V., Gerisch, A., Lolas, G., South, A.P., Chaplain, M.A.J., 2011. Mathematical modeling of cancer cell invasion of tissue: biological insight from mathematical analysis and computational simulation. J. Math. Biol. 63 (1), 141–171.

Andasari, V., Roper, R.T., Swat, M.H., Chaplain, M.A.J., Dadras, S.S., 2012. Integrating intracellular dynamics using CompuCell 3D and Bionetsolver: applications to multiscale modelling of cancer cell growth and invasion. PLoS ONE 7 (3), e33726.

Anderson, A.R. (2005). A hybrid mathematical model of solid tumour invasion: the importance of cell adhesion. Mathematical medicine and biology : a journal of the IMA 22, 163-186.
Anderson, A.R.A., Chaplain, M.A.J., Rejniak, K.A. (Eds.), 2007. Mathematics and Biosciences in InteractionSingle-Cell-Based Models in Biology and Medicine. Birkhäuser Basel, Basel.
Araujo, R.P., McElwain, D.L., 2004. A history of the study of solid tumour growth: the contribution of mathematical modelling. Bull. Math. Biol. 66, 1039–1091.
Aref, H., Tryggvason, G., 1989. Model of Rayleigh-Taylor instability. Phys. Rev. Lett. 62 (7), 749–752.
Bearer, E.L., Lowengrub, J.S., Frieboes, H.B., Chuang, Y.-L., Jin, F., Wise, S.M., Ferrari, M., Agus, D.B., Cristini, V., 2009. Multiparameter computational modeling of tumor invasion. Cancer Res. 69 (10), 4493–4501.
Bhat, R., Bissell, M.J., 2014. Of plasticity and specificity: dialectics of the microenvironment and macroenvironment and the organ phenotype. Wiley interdisciplinary reviews Developmental biology 3 (2), 147–163.
Bocci, F., Kumar Jolly, M., Onuchic, J.N., 2019. A Biophysical Model Uncovers the Size Distribution of Migrating Cell Clusters across Cancer Types. Cancer Res. 79 (21), 5527–5535.
Boghaert, E., Radisky, D.C., Nelson, C.M., Gabhann, F.M., 2014. Lattice-based model of ductal carcinoma in situ suggests rules for breast cancer progression to an invasive state. PLoS Comput. Biol. 10 (12), e1003997.
Bronsert, P., Enderle-Ammour, K., Bader, M., Timme, S., Kuehs, M., Csanadi, A., Kayser, G., Kohler, I., Bausch, D., Hoeppner, J., Hopt, U.T., Keck, T., Stickeler, E., Passlick, B., Schilling, O., Reiss, C.P., Vashist, Y., Brabletz, T., Berger, J., Lotz, J., Olesch, J., Werner, M., Wellner, U.F., 2014. Cancer cell invasion and EMT marker expression: a three-dimensional study of the human cancer-host interface. J. Pathol. 234 (3), 410–422.
Chamseddine, I.M., Rejniak, K.A., 2020. Hybrid modeling frameworks of tumor development and treatment. Wiley Interdiscip. Rev. Syst. Biol. Med. 12, e1461.
Cheung, K., Gabrielson, E., Werb, Z., Ewald, A., 2013. Collective invasion in breast cancer requires a conserved basal epithelial program. Cell 155 (7), 1639–1651.
Christley, S., Alber, M.S., Newman, S.A., Crampin, E.J., 2007. Patterns of mesenchymal condensation in a multiscale, discrete stochastic model. PLoS Comput. Biol. 3 (4), e76.
Clark, A.G., Vignjevic, D.M., 2015. Modes of cancer cell invasion and the role of the microenvironment. Curr. Opin. Cell Biol. 36, 13–22.
Das, A., Monteiro, M., Barai, A., Kumar, S., Sen, S., 2017. MMP proteolytic activity regulates cancer invasiveness by modulating integrins. Sci. Rep. 7, 14219.
Dasgupta, D., Pally, D., Saini, D.K., Bhat, R., Ghosh, A., 2020. Nanomotors Sense Local Physicochemical Heterogeneities in Tumor Microenvironments*. Angew. Chem. 59 (52), 23690–23696.
Di Lullo, G.A., Sweeney, S.M., Körkkö, J., Ala-Kokko, L., San Antonio, J.D., 2002. Mapping the ligand-binding sites and disease-associated mutations on the most abundant protein in the human, type I collagen. The Journal of biological chemistry 277 (6), 4223–4231.
Diambra, L., Senthivel, V.R., Menendez, D.B., Isalan, M., 2015. Cooperativity to increase Turing pattern space for synthetic biology. ACS Synth. Biol. 4 (2), 177–186.
Domschke, P., Trucu, D., Gerisch, A., and M, A.J.C. (2014). Mathematical modelling of cancer invasion: implications of cell adhesion variability for tumour infiltrative growth patterns. Journal of theoretical biology 361, 41-60.
Fang, M., Yuan, J., Peng, C., Li, Y., 2014. Collagen as a double-edged sword in tumor progression. Tumour biology : the journal of the International Society for Oncodevelopmental Biology and Medicine 35 (4), 2871–2882.
Friedl, P., Hegerfeldt, Y., Tusch, M., 2004. Collective cell migration in morphogenesis and cancer. The International journal of developmental biology 48 (5-6), 441–449.
Friedl, P., Locker, J., Sahai, E., Segall, J.E., 2012. Classifying collective cancer cell invasion. Nat. Cell Biol. 14 (8), 777–783.
Friedl, P., Wolf, K., 2008. Tube travel: the role of proteases in individual and collective cancer cell invasion. Cancer Res. 68, 7247–7249.
Gadea, G., Sanz-Moreno, V., Self, A., Godi, A., Marshall, C.J., 2008. DOCK10-mediated Cdc42 activation is necessary for amoeboid invasion of melanoma cells. Current biology : CB 18 (19), 1456–1465.
Glazier, J.A., Graner, F., 1993. Simulation of the differential adhesion driven rearrangement of biological cells. Phys. Rev. E: Stat. Phys. Plasmas Fluids Relat. Interdiscip. Top. 47 (3), 2128–2154.
Gonzalez-Rodriguez, D., Guevorkian, K., Douezan, S., Brochard-Wyart, F., 2012. Soft matter models of developing tissues and tumors. Science 338 (6109), 910–917.
Graner, F., Glazier, J.A., 1992. Simulation of biological cell sorting using a two-dimensional extended Potts model. Phys. Rev. Lett. 69 (13), 2013–2016.
Graves, M.L., Cipollone, J.A., Austin, P., Bell, E.M., Nielsen, J.S., Gilks, C.B., McNagny, K. M., Roskelley, C.D., 2016. The cell surface mucin podocalyxin regulates collective breast tumor budding. Breast cancer research : BCR 18, 11.
Grigore, A.D., Jolly, M.K., Jia, D., Farach-Carson, M.C., Levine, H., 2016. Tumor Budding: The Name is EMT. Partial EMT. Journal of clinical medicine 5.
Haeger, A., Alexander, S., Vullings, M., Kaiser, F.M.P., Veelken, C., Flucke, U., Koehl, G. E., Hirschberg, M., Flentje, M., Hoffman, R.M., et al. (2020). Collective cancer invasion forms an integrin-dependent radioresistant niche. J Exp Med 217.
Harrison, N.C., Diez del Corral, R., Vasiev, B., Heisenberg, C.-P., 2011. Coordination of cell differentiation and migration in mathematical models of caudal embryonic axis extension. PLoS ONE 6 (7), e22700.
Hase, K., Shatney, C., Johnson, D., Trollope, M., Vierra, M., 1993. Prognostic value of tumor "budding" in patients with colorectal cancer. Dis. Colon Rectum 36, 627–635.
Hecht, I., Bar-El, Y., Balmer, F., Natan, S., Tsarfaty, I., Schweitzer, F., Ben-Jacob, E., 2015. Tumor invasion optimization by mesenchymal-amoeboid heterogeneity. Sci. Rep. 5, 10622.
Hodgkinson, A., Chaplain, M.A.J., Domschke, P., Trucu, D., 2018. Computational Approaches and Analysis for a Spatio-Structural-Temporal Invasive Carcinoma Model. Bull. Math. Biol. 80 (4), 701–737.
Huang, B., Jolly, M.K., Lu, M., Tsarfaty, I., Ben-Jacob, E., Onuchic, J.N., 2015. Modeling the Transitions between Collective and Solitary Migration Phenotypes in Cancer Metastasis. Sci. Rep. 5, 17379.
Huang, B., Lu, M., Jolly, M.K., Tsarfaty, I., Onuchic, J., Ben-Jacob, E., 2014. The three-way switch operation of Rac1/RhoA GTPase-based circuit controlling amoeboid-hybrid-mesenchymal transition. Sci. Rep. 4, 6449.
Hynes, R.O., 2009. The extracellular matrix: not just pretty fibrils. Science 326 (5957), 1216–1219.
Ilina, O., Campanello, L., Gritsenko, P.G., Vullings, M., Wang, C., Bult, P., Losert, W., and Friedl, P. (2018). Intravital microscopy of collective invasion plasticity in breast cancer. Disease models & mechanisms 11.
Ilina, O., Gritsenko, P.G., Syga, S., Lippoldt, Jürgen, La Porta, C.A.M., Chepizhko, O., Grosser, S., Vullings, M., Bakker, G.-J., Starruß, Jörn, Bult, P., Zapperi, S., Käs, J.A., Deutsch, A., Friedl, P., 2020. Cell-cell adhesion and 3D matrix confinement determine jamming transitions in breast cancer invasion. Nat. Cell Biol. 22 (9), 1103–1115.
Izaguirre, J.A., Chaturvedi, R., Huang, C., Cickovski, T., Coffland, J., Thomas, G., Forgacs, G., Alber, M., Hentschel, G., Newman, S.A., Glazier, J.A., 2004. CompuCell, a multi-model framework for simulation of morphogenesis. Bioinformatics 20 (7), 1129–1137.
Jain, S., Cachoux, V.M.L., Narayana, G., de Beco, S., D'Alessandro, J., Cellerin, V., Chen, T., Heuze, M.L., Marcq, P., Mege, R.M., et al., 2020. The role of single cell mechanical behavior and polarity in driving collective cell migration. Nat. Phys. 16, 802–809.
Jolly, M.K., Somarelli, J.A., Sheth, M., Biddle, A., Tripathi, S.C., Armstrong, A.J., Hanash, S.M., Bapat, S.A., Rangarajan, A., Levine, H., 2019. Hybrid epithelial/mesenchymal phenotypes promote metastasis and therapy resistance across carcinomas. Pharmacol. Ther. 194, 161–184.
Kedrin, D., Gligorijevic, B., Wyckoff, J., Verkhusha, V.V., Condeelis, J., Segall, J.E., van Rheenen, J., 2008. Intravital imaging of metastatic behavior through a mammary imaging window. Nat. Methods 5 (12), 1019–1021.
Kenny, P.A., Lee, G.Y., Myers, C.A., Neve, R.M., Semeiks, J.R., Spellman, P.T., Lorenz, K., Lee, E.H., Barcellos-Hoff, M.H., Petersen, O.W., et al. (2007). The morphologies of breast cancer cell lines in three-dimensional assays correlate with their profiles of gene expression. Molecular oncology 1, 84-96.
Kiskowski, M.A., Jiang, Y., Alber, M.S., 2004. Role of streams in myxobacteria aggregate formation. Phys. Biol. 1 (3), 173–183.
Krakhmal, N.V., Zavyalova, M.V., Denisov, E.V., Vtorushin, S.V., Perelmuter, V.M., 2015. Cancer Invasion: Patterns and Mechanisms. Acta naturae 7 (2), 17–28.
Kumar, S., Kapoor, A., Desai, S., Inamdar, M.M., Sen, S., 2016. Proteolytic and non-proteolytic regulation of collective cell invasion: tuning by ECM density and organization. Sci. Rep. 6, 19905.
Labernadie, A., Kato, T., Brugues, A., Serra-Picamal, X., Derzsi, S., Arwert, E., Weston, A., Gonzalez-Tarrago, V., Elosegui-Artola, A., Albertazzi, L., et al., 2017. A mechanically active heterotypic E-cadherin/N-cadherin adhesion enables fibroblasts to drive cancer cell invasion. Nat. Cell Biol. 19, 224–237.
Lintz, M., Munoz, A., Reinhart-King, C.A., 2017. The Mechanics of Single Cell and Collective Migration of Tumor Cells. J. Biomech. Eng. 139.
Liu, R., Song, K., Hu, Z., Cao, W., Shuai, J., Chen, S., Nan, H., Zheng, Y., Jiang, X., Zhang, H., Han, W., Liao, Y., Qu, J., Jiao, Y., Liu, L., 2019. Diversity of collective migration patterns of invasive breast cancer cells emerging during microtrack invasion. Phys. Rev. E 99 (6). https://doi.org/10.1103/PhysRevE.99.062403.
Macqueen, J. (1967). Some methods for classification and analysis of multivariate observations. Proc 5th Berkeley Symp Math Stat Probab 1965-66, 281-297.
Madsen, C.D., Sahai, E., 2010. Cancer dissemination–lessons from leukocytes. Dev. Cell 19 (1), 13–26.
Masaki, T., Sugiyama, M., Matsuoka, H., Abe, N., Izumisato, Y., Sakamoto, A., Atomi, Y., 2003. Coexpression of matrilysin and laminin-5 gamma2 chain may contribute to tumor cell migration in colorectal carcinomas. Dig. Dis. Sci. 48, 1262–1267.
Merks, R.M.H., Glazier, J.A., 2006. Dynamic mechanisms of blood vessel growth. Nonlinearity 19 (1), C1–C10.
Metzcar, J., Wang, Y., Heiland, R., Macklin, P., 2019. A Review of Cell-Based Computational Modeling in Cancer Biology. JCO clinical cancer informatics (3), 1–13. https://doi.org/10.1200/CCI.18.00069.
Mikaelian, K.O., 1990. Rayleigh-Taylor and Richtmyer-Meshkov instabilities in multilayer fluids with surface tension. Phys. Rev. A: At. Mol. Opt. Phys. 42 (12), 7211–7225.
Naba, A., Clauser, K.R., Lamar, J.M., Carr, S.A., Hynes, R.O., 2014. Extracellular matrix signatures of human mammary carcinoma identify novel metastasis promoters. eLife 3, e01308.
Nagai, T., Ishikawa, T., Minami, Y., and Nishita, M. (2020). Tactics of cancer invasion: solitary and collective invasion. Journal of biochemistry 167, 347-355.
Nelson, C.M., Bissell, M.J., 2005. Modeling dynamic reciprocity: engineering three-dimensional culture models of breast architecture, function, and neoplastic transformation. Semin. Cancer Biol. 15 (5), 342–352.
Nelson, C.M., VanDuijn, M.M., Inman, J.L., Fletcher, D.A., Bissell, M.J., 2006. Tissue geometry determines sites of mammary branching morphogenesis in organotypic cultures. Science 314 (5797), 298–300.

Newman, S.A., Bhat, R., 2008. Dynamical patterning modules: physico-genetic determinants of morphological development and evolution. Phys. Biol. 5 (1), 015008. https://doi.org/10.1088/1478-3975/5/1/015008.
Newman, S.A., Bhat, R., 2009. Dynamical patterning modules: a "pattern language" for development and evolution of multicellular form. The International journal of developmental biology 53 (5-6), 693–705.
Nieto, M.A., Huang, R.Y., Jackson, R.A., and Thiery, J.P. (2016). Emt: 2016. Cell 166, 21-45.
Nissen, N.I., Karsdal, M., Willumsen, N., 2019. Collagens and Cancer associated fibroblasts in the reactive stroma and its relation to Cancer biology. Journal of experimental & clinical cancer research : CR 38, 115.
O'Brien, J., Lyons, T., Monks, J., Lucia, M.S., Wilson, R.S., Hines, L., Man, Y.-gao., Borges, V., Schedin, P., 2010. Alternatively activated macrophages and collagen remodeling characterize the postpartum involuting mammary gland across species. The American journal of pathology 176 (3), 1241–1255.
Olivares, O., Mayers, J.R., Gouirand, V., Torrence, M.E., Gicquel, T., Borge, L., Lac, S., Roques, J., Lavaut, M.-N., Berthezène, P., Rubis, M., Secq, V., Garcia, S., Moutardier, V., Lombardo, D., Iovanna, J.L., Tomasini, R., Guillaumond, F., Vander Heiden, M.G., Vasseur, S., 2017. Collagen-derived proline promotes pancreatic ductal adenocarcinoma cell survival under nutrient limited conditions. Nat. Commun. 8 (1). https://doi.org/10.1038/ncomms16031.
Oyelade, J., Isewon, I., Oladipupo, F., Aromolaran, O., Uwoghiren, E., Ameh, F., Achas, M., Adebiyi, E., 2016. Clustering Algorithms: Their Application to Gene Expression Data. Bioinf. Biol. Insights 10, 237–253.
Ozik, J., Collier, N., Heiland, R., An, G., Macklin, P., 2019. Learning-accelerated discovery of immune-tumour interactions. Mol. Syst. Des. Eng. 4 (4), 747–760.
Pally, D., Pramanik, D., Bhat, R., 2019. An Interplay Between Reaction-Diffusion and Cell-Matrix Adhesion Regulates Multiscale Invasion in Early Breast Carcinomatosis. Front. Physiol. 10.
Pally, D., Pramanik, D., Hussain, S., Verma, S., Srinivas, A., Kumar, R.V., Everest-Dass, A., Bhat, R., 2021. Heterogeneity in 2,6-Linked Sialic Acids Potentiates Invasion of Breast Cancer Epithelia. ACS Cent. Sci. 7 (1), 110–125.
Paňková, K., Rösel, D., Novotný, M., Brábek, J., 2010. The molecular mechanisms of transition between mesenchymal and amoeboid invasiveness in tumor cells. Cellular and molecular life sciences : CMLS 67 (1), 63–71.
Patsialou, A., Bravo-Cordero, J.J., Wang, Y., Entenberg, D., Liu, H., Clarke, M., Condeelis, J.S., 2013. Intravital multiphoton imaging reveals multicellular streaming as a crucial component of in vivo cell migration in human breast tumors. Intravital 2 (2), e25294. https://doi.org/10.4161/intv.25294.
Peng, L., Trucu, D., Lin, P., Thompson, A., Chaplain, M.A.J., 2017. A Multiscale Mathematical Model of Tumour Invasive Growth. Bull. Math. Biol. 79 (3), 389–429.
Pérez-González, C., Alert, R., Blanch-Mercader, C., Gómez-González, M., Kolodziej, T., Bazellieres, E., Casademunt, J., Trepat, X., 2019. Active wetting of epithelial tissues. Nat. Phys. 15 (1), 79–88.
Petrova, E., Zielinski, V., Bolm, L., Schreiber, C., Knief, J., Thorns, C., Bronsert, P., Timme-Bronsert, S., Bausch, D., Perner, S., et al. (2019). Tumor budding as a prognostic factor in pancreatic ductal adenocarcinoma. Virchows Archiv : an international journal of pathology.
Pickup, M.W., Mouw, J.K., and Weaver, V.M. (2014). The extracellular matrix modulates the hallmarks of cancer. EMBO reports 15, 1243-1253.
Postlethwaite, A.E., Seyer, J.M., Kang, A.H., 1978. Chemotactic attraction of human fibroblasts to type I, II, and III collagens and collagen-derived peptides. PNAS 75 (2), 871–875.
Prall, F., 2007. Tumour budding in colorectal carcinoma. Histopathology 50 (1), 151–162.
Prall, F., Nizze, H., Barten, M., 2005. Tumour budding as prognostic factor in stage I/II colorectal carcinoma. Histopathology 47 (1), 17–24.
Prall, F., Ostwald, C., 2007. High-degree tumor budding and podia-formation in sporadic colorectal carcinomas with K-ras gene mutations. Hum Pathol 38 (11), 1696–1702.
Prall, F., Ostwald, C., Linnebacher, M., 2009. Tubular invasion and the morphogenesis of tumor budding in colorectal carcinoma. Hum Pathol 40 (10), 1510–1512.
Ramis-Conde, I., Drasdo, D., Anderson, A.R., Chaplain, M.A., 2008. Modeling the influence of the E-cadherin-beta-catenin pathway in cancer cell invasion: a multiscale approach. Biophys. J . 95, 155–165.
Reher, D., Klink, B., Deutsch, A., Voss-Bohme, A., 2017. Cell adhesion heterogeneity reinforces tumour cell dissemination: novel insights from a mathematical model. Biology direct 12, 18.
Ridley, A.J., 2015. Rho GTPase signalling in cell migration. Curr. Opin. Cell Biol. 36, 103–112.
Roussos, E.T., Condeelis, J.S., Patsialou, A., 2011. Chemotaxis in cancer. Nature reviews. Cancer 11 (8), 573–587.
Sadati, M., Taheri Qazvini, N., Krishnan, R., Park, C.Y., Fredberg, J.J., 2013. Collective migration and cell jamming. Differentiation; research in biological diversity 86 (3), 121–125.
Salhia, B., Trippel, M., Pfaltz, K., Cihoric, N., Grogg, A., Lädrach, C., Zlobec, I., Tapia, C., 2015. High tumor budding stratifies breast cancer with metastatic properties. Breast Cancer Res. Treat. 150 (2), 363–371.
Sanz-Moreno, V., Gadea, G., Ahn, J., Paterson, H., Marra, P., Pinner, S., Sahai, E., Marshall, C.J., 2008. Rac activation and inactivation control plasticity of tumor cell movement. Cell 135 (3), 510–523.
Schuppan, D., Schmid, M., Somasundaram, R., Ackermann, R., Ruehl, M., Nakamura, T., Riecken, E., 1998. Collagens in the liver extracellular matrix bind hepatocyte growth factor. Gastroenterology 114 (1), 139–152.
Scianna, M., Preziosi, L., 2013. Cellular Potts models multiscale extensions and biological applications. In Chapman & Hall/CRC mathematical and computational biology series. CRC Press, Boca Raton, FL.
Scianna, M., Preziosi, L., Wolf, K., 2013. A Cellular Potts Model simulating cell migration on and in matrix environments. Mathematical biosciences and engineering : MBE 10, 235–261.
Somasundaram, R., Ruehl, M., Schaefer, B., Schmid, M., Ackermann, R., Riecken, E.O., Zeitz, M., Schuppan, D., 2002. Interstitial collagens I, III, and VI sequester and modulate the multifunctional cytokine oncostatin M. The Journal of biological chemistry 277 (5), 3242–3246.
Somasundaram, R., Ruehl, M., Tiling, N., Ackermann, R., Schmid, M., Riecken, E.O., Schuppan, D., 2000. Collagens serve as an extracellular store of bioactive interleukin 2. The Journal of biological chemistry 275 (49), 38170–38175.
Swat, M.H., Thomas, G.L., Belmonte, J.M., Shirinifard, A., Hmeljak, D., Glazier, J.A., 2012. Multi-scale modeling of tissues using CompuCell 3D. Methods Cell Biol. 110, 325–366.
Szabo, A., Merks, R.M., 2013. Cellular potts modeling of tumor growth, tumor invasion, and tumor evolution. Front. Oncol. 3, 87.
Tlili, S., Gauquelin, E., Li, B., Cardoso, O., Ladoux, B., Delanoë-Ayari, Hélène, Graner, F., 2018. Collective cell migration without proliferation: density determines cell velocity and wave velocity. R. Soc. Open Sci. 5 (5), 172421. https://doi.org/10.1098/rsos.172421.
Trepat, X., Fredberg, J.J., 2011. Plithotaxis and emergent dynamics in collective cellular migration. Trends Cell Biol. 21 (11), 638–646.
van Zijl, F., Krupitza, G., Mikulits, W., 2011. Initial steps of metastasis: cell invasion and endothelial transmigration. Mutat. Res. 728 (1-2), 23–34.
Vedula, S.R.K., Hirata, H., Nai, M.H., Brugués, A., Toyama, Y., Trepat, X., Lim, C.T., Ladoux, B., 2014. Epithelial bridges maintain tissue integrity during collective cell migration. Nat. Mater. 13 (1), 87–96.
Vedula, S.R.K., Leong, M.C., Lai, T.L., Hersen, P., Kabla, A.J., Lim, C.T., Ladoux, B., 2012. Emerging modes of collective cell migration induced by geometrical constraints. PNAS 109 (32), 12974–12979.
Wolf, K., Wu, Y.I., Liu, Y., Geiger, Jörg, Tam, E., Overall, C., Stack, M.S., Friedl, P., 2007. Multi-step pericellular proteolysis controls the transition from individual to collective cancer cell invasion. Nat. Cell Biol. 9 (8), 893–904.
Xu, S., Xu, H., Wang, W., Li, S., Li, H., Li, T., Zhang, W., Yu, X., Liu, L., 2019. The role of collagen in cancer: from bench to bedside. Journal of translational medicine 17, 309.
Yang, Y., Zheng, H., Zhan, Y., Fan, S., 2019. An emerging tumor invasion mechanism about the collective cell migration. American journal of translational research 11, 5301–5312.
Zhang, Y., Thomas, G.L., Swat, M., Shirinifard, A., Glazier, J.A., Mathe, J., 2011. Computer simulations of cell sorting due to differential adhesion. PLoS ONE 6 (10), e24999.
Zhao, S., Sun, J., Shimizu, K., Kadota, K., 2018. Silhouette Scores for Arbitrary Defined Groups in Gene Expression Data and Insights into Differential Expression Results. Biological procedures online 20, 5.